45. Stevens J K, Trogadis J (1986) Reconstructive three-dimensional electron microscopy. A routine biologic tool. *Anal Quant Cytol Histol* 8: 102–107.
46. Stevens J K, Davis T L, Friedman N, Sterling P (1980) A systematic approach to reconstructing microcircuitry by electron microscopy of serial sections. *Brain Res* 2: 265–293.
47. Harris K M, Stevens J K (1988) Dendritic spines of rat cerebellar Purkinje cells: serial electron microscopy with reference to their biophysical characteristics. *J Neurosci* 8: 4455–4469.
48. Briggman K L, Helmstaedter M, Denk W (2011) Wiring specificity in the direction-selectivity circuit of the retina. *Nature* 471: 183–188.
49. Terasaki M, Shemesh T, Kasthuri N, Klemm R W, Schalek R, Hayworth K J, Hand A R, Yankova M, Huber G, Lichtman J W, Rapoport T A, Kozlov M M (2013) Stacked endoplasmic reticulum sheets are connected by helicoidal membrane motifs. *Cell* 154: 285–296.
50. Bock D D, Lee W C, Kerlin A M, Andermann M L, Hood G, Wetzel A W, Yurgenson S, Soucy E R, Kim H S, Reid R C (2011) Network anatomy and in vivo physiology of visual cortical neurons. *Nature* 471: 177–182.
51. Kuwajima M, Mendenhall J M, Lindsey L F, Harris K M (2013) Automated transmission-mode scanning electron microscopy (tSEM) for large volume analysis at nanoscale resolution. *PloS One* 8: e59573.
52. Schalek R, Kasthuri N, Hayworth K, Berger D, Tapia J, Morgan J, Turaga S C, Fagerholm E, Seung H S, Lichtman J W (2011) Development of high-throughput, high-resolution 3D reconstruction of large-volume biological tissue using automated tape collection ultramicrotomy and scanning electron microscopy. *Microsc Microanal* 17: 2.
53. Denk W, Horstmann H (2004) Serial block-face scanning electron microscopy to reconstruct three-dimensional tissue nanostructure. *PLoS Biol* 2: e329.
54. Knott G, Marchman H, Wall D, Lich B (2008) Serial section scanning electron microscopy of adult brain tissue using focused ion beam milling. *J Neurosci* 28: 2959–2964.
55. Zhang L, Kaneko S, Kikuchi K, Sano A, Maeda M, Kishino A, Shibata S, Mukaino M, Toyama Y, Liu M, Kimura T, Okano H, Nakamura M (2014) Rewiring of regenerated axons by combining treadmill training with semaphorin3A inhibition. *Mol Brain* 7: 14.
56. Takano M, Kawabata S, Komaki Y, Shibata S, Hikishima K, Toyama Y, Okano H, Nakamura M (2014) Inflammatory cascades mediate synapse elimination in spinal cord compression. *J Neuroinflammation* 11: 40.
57. Numasawa-Kuroiwa Y, Okada Y, Shibata S, Kishi N, Akamatsu W, Shoji M, Nakanishi A, Oyama M, Osaka H, Inoue K, Takahashi K, Yamanaka S, Kosaki K, Takahashi T, Okano H (2014) Involvement of ER stress in dysmyelination of Pelizaeus–Merzbacher disease with PLP1 missense mutations shown by iPSC-derived oligodendrocytes. *Stem Cell Rep* 2: 648–661.
58. Murota Y, Ishizu H, Nakagawa S, Iwasaki Y W, Shibata S, Kamatani M K, Saito K, Okano H, Siomi H, Siomi M C (2014) Yb integrates piRNA intermediates and processing factors into perinuclear bodies to enhance piRISC assembly. *Cell Rep* 8: 103–113.
59. Nishimoto Y, Nakagawa S, Hirose T, Okano H J, Takao M, Shibata S, Suyama S, Kuwako K, Imai T, Murayama S, Suzuki N, Okano H (2013) The long non-coding RNA nuclear-enriched abundant transcript 1_2 induces paraspeckle formation in the motor neuron during the early phase of amyotrophic lateral sclerosis. *Mol Brain* 6: 31.
60. Takano M, Hikishima K, Fujiyoshi K, Shibata S, Yasuda A, Konomi T, Hayashi A, Baba H, Honke K, Toyama Y, Okano H, Nakamura M (2012) MRI characterization of paranodal junction failure and related spinal cord changes in mice. *PloS One* 7: e52904.
61. Yasuda A, Tsuji O, Shibata S, Nori S, Takano M, Kobayashi Y, Takahashi Y, Fujiyoshi K, Hara C M, Miyawaki A, Okano H J, Toyama Y, Nakamura M, Okano H (2011) Significance of remyelination by neural stem/progenitor cells transplanted into the injured spinal cord. *Stem Cells* 29: 1983–1994.
62. Nagoshi N, Shibata S, Hamanoue M, Mabuchi Y, Matsuzaki Y, Toyama Y, Nakamura M, Okano H (2011) Schwann cell plasticity after spinal cord injury shown by neural crest lineage tracing. *Glia* 59: 771–784.
63. Tada H, Okano H J, Takagi H, Shibata S, Yao I, Matsumoto M, Saiga T, Nakayama K I, Kashima H, Takahashi T, Setou M, Okano H (2010) Fbxo45, a novel ubiquitin ligase, regulates synaptic activity. *J Biol Chem* 285: 3840–3849.
64. Shibata S, Yasuda A, Renault-Mihara F, Suyama S, Katoh H, Inoue T, Inoue Y U, Nagoshi N, Sato M, Nakamura M, Akazawa C, Okano H (2010) Sox10-Venus mice: a new tool for real-time labeling of neural crest lineage cells and oligodendrocytes. *Mol Brain* 3: 31.
65. Kumagai G, Okada Y, Yamane J, Nagoshi N, Kitamura K, Mukaino M, Tsuji O, Fujiyoshi K, Katoh H, Okada S, Shibata S, Matsuzaki Y, Toh S, Toyama Y, Nakamura M, Okano H (2009) Roles of ES cell-derived gliogenic neural stem/progenitor cells in functional recovery after spinal cord injury. *PloS One* 4: e7706.

Cell Reports
Report

Yb Integrates piRNA Intermediates and Processing Factors into Perinuclear Bodies to Enhance piRISC Assembly

Yukiko Murota,[1,2,6] Hirotsugu Ishizu,[3,6] Shinichi Nakagawa,[4] Yuka W. Iwasaki,[2] Shinsuke Shibata,[5] Miharu K. Kamatani,[2] Kuniaki Saito,[2] Hideyuki Okano,[5] Haruhiko Siomi,[2] and Mikiko C. Siomi[3,*]
[1]Institute for Genome Research, University of Tokushima, Tokushima 770-8503, Japan
[2]Department of Molecular Biology, Keio University School of Medicine, Tokyo 160-8582, Japan
[3]Department of Biological Sciences, Graduate School of Science, The University of Tokyo, Tokyo 113-0032, Japan
[4]RIKEN, Wako, Saitama 351-0198, Japan
[5]Department of Biomedical Physiology, Keio University School of Medicine, Tokyo 160-8582, Japan
[6]Co-first author
*Correspondence: siomim@bs.s.u-tokyo.ac.jp
http://dx.doi.org/10.1016/j.celrep.2014.05.043

SUMMARY

PIWI-interacting RNAs (piRNAs) direct Piwi to repress transposons and maintain genome integrity in *Drosophila* ovarian somatic cells. piRNA maturation and association with Piwi occur at perinuclear Yb bodies, the centers of piRNA biogenesis. Here, we show that piRNA intermediates arising from the piRNA cluster *flamenco* (*flam*) localize to perinuclear foci adjacent to Yb bodies, termed Flam bodies. RNAi-based screening of piRNA factors revealed that Flam body formation depends on Yb, the core component of Yb bodies, while Piwi and another Yb body component, Armitage, are dispensable for formation. Abolishing the RNA-binding activity of Yb disrupts both Flam bodies and Yb bodies. Yb directly binds *flam*, but not transcripts from neighboring protein-coding genes. Thus, Yb integrates piRNA intermediates and piRNA processing factors selectively into Flam bodies and Yb bodies, respectively. We suggest that Yb is a key upstream factor in the cytoplasmic phase of the piRNA pathway in ovarian somatic cells.

INTRODUCTION

PIWI-interacting RNAs (piRNAs) are small noncoding RNAs of 23–30 nt that are enriched in animal germlines. piRNAs specifically interact with PIWI proteins to form piRNA-induced silencing complexes (piRISCs) and direct them to repress transposons and thus maintain genome integrity in the gonads (Ishizu et al., 2012; Juliano et al., 2011; Siomi et al., 2011). Loss-of-function mutations of PIWI proteins or piRNA biogenesis impairment cause derepression of transposons, leading to defects in gametogenesis and sterility (Aravin et al., 2007; Khurana and Theurkauf, 2010).

Drosophila express three PIWI proteins: Piwi, Aubergine (Aub), and AGO3 (Siomi et al., 2011). In germ cells in the ovaries, primary piRNAs originate from intergenic piRNA clusters through the primary piRNA processing pathway in a Dicer-independent fashion and are loaded onto Piwi and Aub. Following this, Piwi localizes to the nucleus to mediate transposon silencing. In contrast, Aub localizes to the cytoplasm, where it plays a role in the piRNA amplification cycle cooperating with AGO3 through reciprocal RNA cleavage that depends on PIWI-Slicer (endonuclease) activity (Brennecke et al., 2007; Gunawardane et al., 2007; Ishizu et al., 2012; Malone et al., 2009). In this system, transposon transcripts in both sense and antisense orientations are consumed as piRNA precursors; thus, transposon silencing and piRNA production occur simultaneously, enabling a constant supply of piRNAs in cells.

Somatic cells in ovaries express Piwi, but not Aub or AGO3; therefore, they fail to amplify piRNAs. Thus, all piRNAs are primary and are specifically loaded onto Piwi (Ishizu et al., 2012). The Piwi-piRNA complex is then translocated to the nucleus, in which it implements transcriptional silencing in cooperation with cofactors such as Maelstrom and DmGTSF1/Asterix (Dönertas et al., 2013; Muerdter et al., 2013; Ohtani et al., 2013; Sienski et al., 2012). Whether Piwi in germ cells analogously collaborates with Maelstrom and DmGTSF1/Asterix to achieve transposon repression remains unknown.

Investigation of the primary piRNA pathway using a cultured *Drosophila* ovarian somatic cell (OSC) line and fly ovaries has revealed that perinuclear Yb bodies are the centers for piRNA processing and piRISC formation in ovarian somatic cells (Olivieri et al., 2010; Saito et al., 2010). Protein constituents of Yb bodies include Yb, Armitage (Armi), Shutdown (Shu), Sister of Yb (SoYb) and Vreteno (Vret), all of which contain domains associated with RNA metabolism; for instance, Yb shows significant similarity to DEAD-box proteins and contains a Tudor (Tud) domain, whereas Vret contains two Tud domains and an RNA-recognition motif (Ishizu et al., 2012). Armi belongs to the Upf1p family of ATP-dependent RNA helicase (Cook et al., 2004). Loss of Yb body components prevents accumulation of primary piRNAs in the

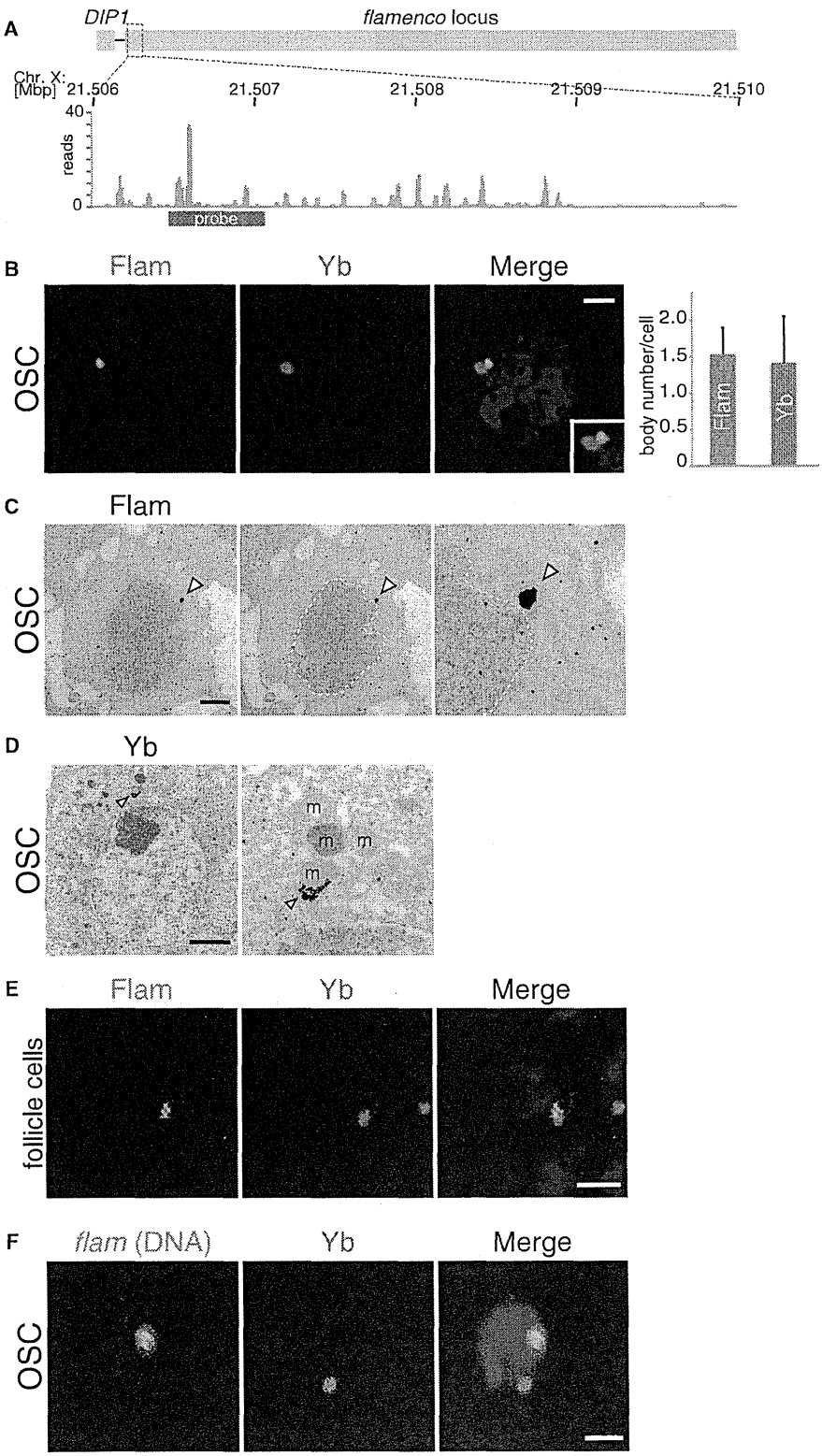

(legend on next page)

soma; thus, they are all required for primary piRNA biogenesis and gonadal development (Haase et al., 2010; Handler et al., 2011; Olivieri et al., 2010, 2012; Qi et al., 2011; Saito et al., 2010; Szakmary et al., 2009; Zamparini et al., 2011).

Nascent, piRNA-unloaded Piwi in OSCs interacts with Armi and Yb, and the resultant complex associates with piRNA intermediates in Yb bodies (Olivieri et al., 2010; Saito et al., 2010). Depletion of Yb disrupts Yb bodies, liberating other components into the cytosol. Under these conditions, Piwi and Armi still associate, although the heterodimer does not contain piRNA intermediates. As a result, piRISC formation fails. It is likely that Yb is at the top of the hierarchy for Yb body formation and piRISC formation and that Armi, although categorized as an RNA helicase based on peptide sequence similarity, binds RNA substrates (piRNA intermediates) upon localization to Yb bodies.

Zucchini (Zuc), a phospholipase D superfamily member, is a single-strand-specific endonuclease required for converting piRNA intermediates to mature piRNAs (Ipsaro et al., 2012; Nishimasu et al., 2012). Depletion of Zuc in OSCs results in dispersal of Yb bodies, because piRNA-unloaded Piwi is stalled and fails to localize to the nucleus (Saito et al., 2010). Without Zuc, an excess of unprocessed piRNA intermediates accumulate in OSCs as ribonucleoprotein (RNP) complexes with Armi, Yb, and Piwi; as a result, few piRNAs are produced (Haase et al., 2010; Nishimasu et al., 2012; Saito et al., 2010). These defects can be rescued by ectopic expression of wild-type (WT) Zuc, but not by ectopic expression of endonuclease-deficient Zuc mutants (Nishimasu et al., 2012). Zuc has a mitochondrial targeting signal at the N terminus, and indeed mouse Zuc (also known as MitoPLD) localizes to the outer membranes of mitochondria, facing into the cytosol in mammalian cells (Choi et al., 2006). Zuc signals in OSCs can be detected in close proximity to Yb bodies (Saito et al., 2010), as pi-bodies and piP-bodies, which are considered to be the sites of piRNA biogenesis in mouse testis, are located in intermitochondrial regions (Pillai and Chuma, 2012). This type of intracellular architectural arrangement might raise the rates of Zuc-mediated conversion of piRNA intermediates to mature piRNAs in the cells.

The functions of piRNA protein factors have been well studied. In contrast, the cell biology of piRNA precursors is poorly understood. Therefore, in this study, we performed RNA-fluorescence in situ hybridization (RNA-FISH) in OSCs to visualize RNA transcripts arising from the *flamenco* (*flam*) piRNA cluster. *flam* is the main source of primary piRNAs in OSCs and somatic follicle cells in *Drosophila* ovaries (Brennecke et al., 2007; Malone et al., 2009; Saito et al., 2009). A P-element insertion in *flam* causes derepression of transposons such as *gypsy* and piRNA loss in mutant follicle cells (Brennecke et al., 2007; Mével-Ninio et al., 2007). RNA-FISH showed that *flam* transcripts are condensed into perinuclear foci adjacent to Yb bodies, which we termed Flam bodies. Recently, a similar type of body named "Dot COM" was reported (Dennis et al., 2013). The similarities and differences between Flam bodies and Dot COM will be described below. RNAi-based screening of piRNA factors revealed that Flam body formation depends on Yb, the core component of Yb bodies, while Piwi and another Yb body component, Armi, are dispensable for the assembly. Depletion of Zuc, which causes excessive accumulation of unprocessed piRNA intermediates (Haase et al., 2010; Nishimasu et al., 2012), results in the dispersion of Flam bodies, which overlap considerably with Yb bodies. Abolishing the RNA-binding activity of Yb disrupts both Flam bodies and Yb bodies. Yb directly binds *flam* transcripts, but not the transcripts of a neighboring protein-coding gene, *DIP1*. Thus, Yb integrates piRNA intermediates and piRNA processing factors selectively into Flam bodies and Yb bodies, respectively. We propose that Yb is a key upstream factor in the cytoplasmic phase of the piRNA pathway in the ovarian soma.

RESULTS

flam Transcripts Are Localized to Perinuclear Flam Bodies in Ovarian Soma

To examine the cellular localization of *flam* transcripts in OSCs, we performed RNA-FISH using a *flam*-specific riboprobe complementary to the 5′ region of the *flam* transcript (Figure 1A). This region produces a substantial amount of primary piRNAs in OSCs (Saito et al., 2010) (Figure 1A). By RNA-FISH, perinuclear, punctate signals were observed, suggesting that the *flam*-piRNA precursors/intermediates concentrate at the cytoplasmic bodies (Figures 1B and S1A). A recent report showed that *flam/COM* transcripts (*flam* is also known as *COM*) are enriched in a single nuclear focus, termed Dot COM (Dennis et al., 2013). However, using electron microscopy in situ hybridization (EM-ISH), we detected *flam* signals in the cytoplasm (Figures 1C and S1B). Fluorescence quantification analysis revealed that the average number of Flam bodies per cell was 1.5 (Figure 1B). Signals from RNA-FISH riboprobes that were used originally by Dennis et al. (COM 508 and 527) (Dennis et al., 2013) coincided with the *flam* signals (Figure S1C). Hereinafter,

Figure 1. Flam Bodies Localize Adjacent to Yb Bodies in *Drosophila* Ovarian Soma

(A) Schematic drawing of the genomic *flam* locus and an upstream protein-coding gene *DIP1* on chromosome X. Mature piRNAs uniquely mapping to the 5′ region of the *flam* locus corresponding to 21,506,000 to 21,510,000 on chromosome X (Saito et al., 2009) are shown by blue bars. A 583 nt riboprobe for RNA-FISH complementary to the *flam* transcripts is shown by a magenta box (probe) (chrX: 21,506,472–21,507,054).

(B) Flam body (green) and Yb body (magenta) in OSCs visualized by RNA-FISH and immunofluorescence using anti-Yb antibody, respectively. The nucleus is stained with DAPI (blue). Scale bar, 2 μm. The numbers of Flam bodies and Yb bodies were determined by quantification analysis of *flam* and Yb signals in OSCs (n = 20).

(C) Electron microscope in situ hybridization using the probe shown in (A) detects a *flam* signal (white arrowhead) in the cytoplasm of OSC. The far-right image is an enlarged image of the middle image (partial). A white dot line shows where the nucleus is. Scale bar, 2 μm.

(D) Immunoelectron microscopy using anti-Yb antibody shows a perinuclear Yb body in an OSC (white arrowhead). The right-hand image is an enlarged image of the left-side image (partial). m, mitochondria. Scale bar, 2 μm.

(E) Flam body (green) and Yb bodies (magenta) in follicular cells of *Drosophila* ovaries. The nuclei are stained with DAPI (blue). Scale bar, 2 μm.

(F) The *flam* loci (green) in the nucleus and Yb body (magenta) in the cytoplasm. The nucleus is stained with DAPI (blue). Scale bar, 2 μm.

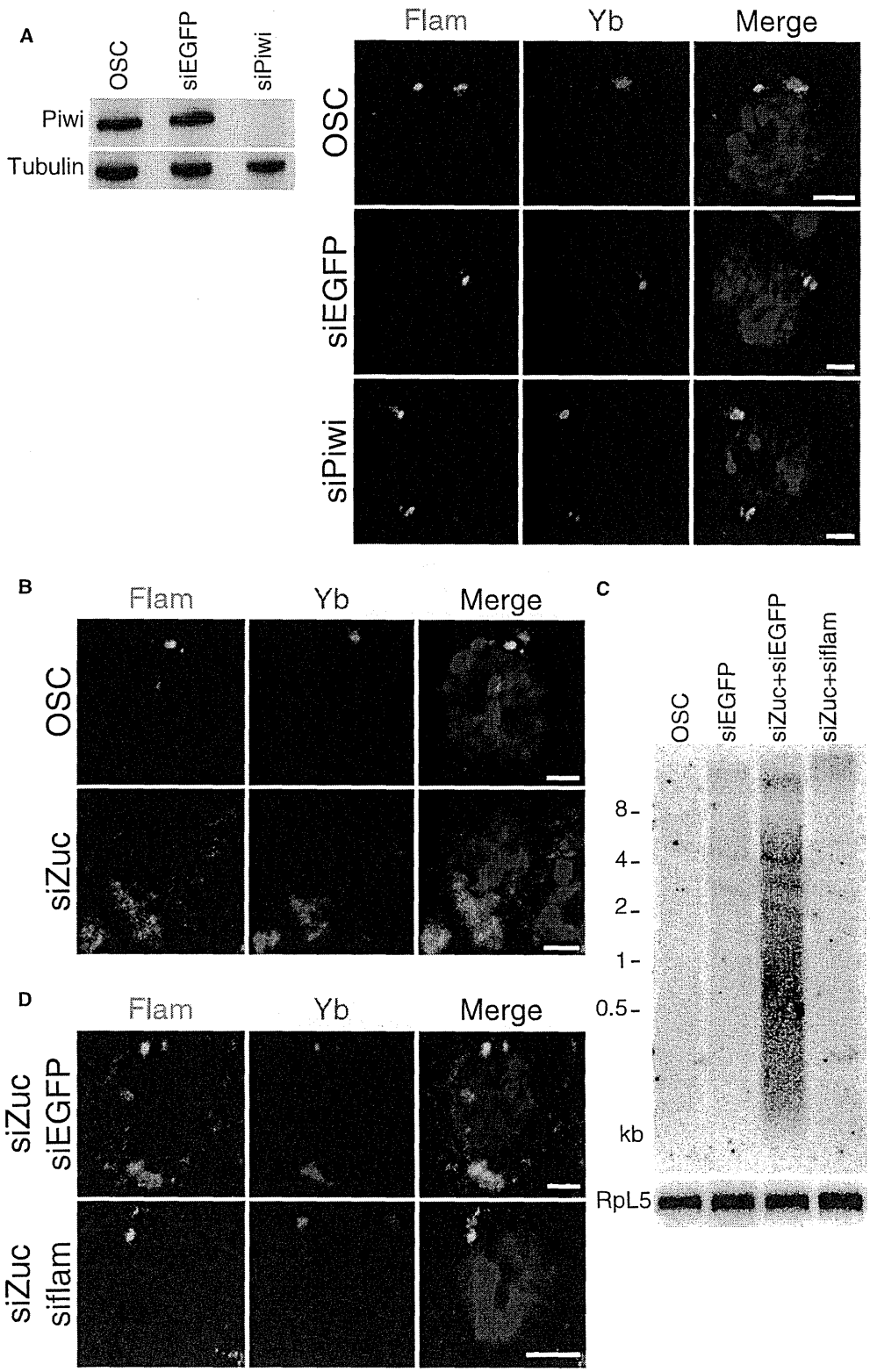

(legend on next page)

we refer to the *flam*-positive, perinuclear bodies as Flam bodies.

Flam bodies appear to be similar to Yb bodies, both in size and number. Therefore, we set out to understand the spatial relationship between Flam bodies and Yb bodies in OSCs by combining *flam* RNA-FISH and immunofluorescence using an anti-Yb antibody that we raised in this study (Figure S1D). Immunoelectron microscopy using the antibody confirmed the perinuclear localization of Yb bodies (Figure 1D). Flam bodies were frequently located adjacent to Yb bodies and tended to be closer to the nucleus than Yb bodies (Figures 1B and S1A). The average number of Yb bodies was similar to that of Flam bodies (1.4 per cell) (Figure 1B). Both signals were also detected in the somatic follicle cells of *Drosophila* ovaries (Figures 1E and S1E). Thus, they are not specific for cultured cells. In *flam* mutant follicle cells, Flam bodies were not detected, confirming the specificity of the RNA-FISH probe (Figure S1F). EM-ISH confirmed the cytoplasmic localization of Flam bodies in follicle cells (Figure S1G). DNA-FISH (Figure S1H) was conducted concomitantly with immunofluorescence using the anti-Yb antibody. No spatial correlation was found between *flam* nuclear foci and Yb bodies (Figures 1F and S1I).

Flam Bodies Are Not the Sites of Mature piRNA Accumulation

It is possible that mature *flam*-piRNAs, rather than their intermediates and/or full transcripts, might be the major components of Flam bodies. To examine this, we visualized Flam bodies and Yb bodies in Piwi-depleted OSCs. Loss of Piwi decreased the level of mature piRNAs drastically (Saito et al., 2009, 2010). This was because Piwi is the sole protein loaded with mature piRNAs in OSCs and, thus, piRNAs are destabilized without Piwi. If mature piRNAs were the major RNA components of Flam bodies, Piwi depletion would cause disappearance of these bodies. However, they were unaffected by Piwi depletion (Figure 2A). These results indicate that Piwi is dispensable for Flam body formation and that Flam bodies are not the sites of mature piRNA storage.

piRNA Intermediates Concentrate in Flam Bodies

Depletion of Zuc caused Yb body dispersion and stalling of Piwi at Yb bodies (Saito et al., 2010). This particular fraction of Piwi was associated with few or no mature piRNAs, although the Armi complex containing Yb and Piwi still bound piRNA intermediates (Saito et al., 2010). These phenomena correlate well with our recent finding that Zuc is the endoribonuclease necessary for converting piRNA intermediates to mature piRNAs (i.e., piRNA maturation) (Nishimasu et al., 2012). We asked if Flam body formation is affected by loss of Zuc. RNA-FISH in Zuc-depleted OSCs showed that Flam bodies were dispersed similarly to Yb bodies (Figure 2B). Interestingly, the two fluorescent signals were superimposed (Figure 2B). We speculated that the increased level of piRNA intermediates might have caused the superimposition. To examine this, northern blotting was performed to detect *flam* transcripts using probes designed to recognize the 5′ end region of *flam* (the "probe" region in Figure 1A). In naive OSCs, a smeary signal for *flam* transcripts was only slightly detected, although Flam bodies were clearly visible by RNA-FISH (Figures 2B and 2C). However, partial *flam* transcripts, being several hundred to 4,000 nt in length, were aberrantly accumulated upon Zuc depletion (Figures 2C and S2A) in agreement with our earlier observation (Nishimasu et al., 2012). The corresponding signal decreased after treatment of the cells with *flam* small interfering RNAs (siRNAs) targeting the probed *flam* region (Figures 2C and S2A). These results suggest that the smeared northern blot signal mostly reflects *flam*-piRNA intermediates. After transfection of cells with *flam* siRNAs, the fuzzy fluorescent signals of Yb bodies and Flam bodies returned to normal, as in naive OSCs (Figure 2D). We suggest that Flam bodies are where *flam*-piRNA intermediates concentrate and that piRNA intermediates originating from loci other than *flam* would be minor. Treatment of normal OSCs with *flam* siRNAs did not disrupt Flam bodies (Figure S2B) and barely affected the levels of *flam* transcripts (Figure S2C), although *flam* siRNAs effectively downregulated *flam* transcripts in Zuc-depleted cells (Figure 2C). *flam* siRNAs were designed to target the region corresponding to the *flam* RNA-FISH probe (Figure 1A). Thus, it is plausible that *flam*-piRNA intermediates at Flam bodies would not be accessible to the RNAi machinery under normal conditions likely due to the compactness of the bodies.

Yb Is Necessary for Formation of Both Yb Bodies and Flam Bodies

Depletion of Yb, but not other Yb body components, disrupts Yb body formation (Handler et al., 2011; Saito et al., 2010). We examined if depletion of Yb would affect Flam body formation. Interestingly, neither Flam bodies nor Yb bodies were detected in the cells (Figures 3A and S3A). Expression of siRNA-resistant Yb (Yb WT-r) restored the formation of both structures (Figures 3A and S3A). Thus, Flam bodies depend on Yb for their formation as do Yb bodies. *Yb* mutant follicle cells contain neither Flam bodies nor Yb bodies (Figure S3B). Depletion of Armi and Vret, other components of Yb bodies (Olivieri et al., 2010), affected neither Flam nor Yb body formation (Figure S3C and data not

Figure 2. Depletion of Zuc, but Not of Piwi, Affects Yb Body and Flam Body Formation

(A) Western blotting shows the efficiency of Piwi depletion. Piwi siRNA (siPiwi) has little effect on Flam body (green) and Yb body (magenta) formation. Enhanced GFP siRNA (siEGFP) was used as a negative control. Nuclei are stained with DAPI (blue). Scale bar, 2 μm.

(B) Transfection of OSCs with Zuc siRNA (siZuc) led to superimposition of Flam bodies (green) with Yb bodies (magenta). Nuclei are stained with DAPI (blue). Scale bar, 2 μm.

(C) Northern blotting shows that transfection of OSCs with Zuc siRNA (siZuc) induces aberrant accumulation of *flam*-piRNA intermediates in OSCs. Transfection of Zuc-depleted OSCs with *flam* siRNAs (siflam) targeting the probed *flam* region downregulates the expression of *flam*-piRNA intermediates. Enhanced GFP siRNA (siEGFP) was used as a negative control. *RpL5* mRNA was visualized as a loading control.

(D) Flam bodies (green) and Yb bodies (magenta) in Zuc-depleted OSCs. Either enhanced GFP siRNA (siEGFP) or *flam* siRNA (siflam) was transfected into OSCs. Nuclei are stained with DAPI (blue). Scale bar, 2 μm.

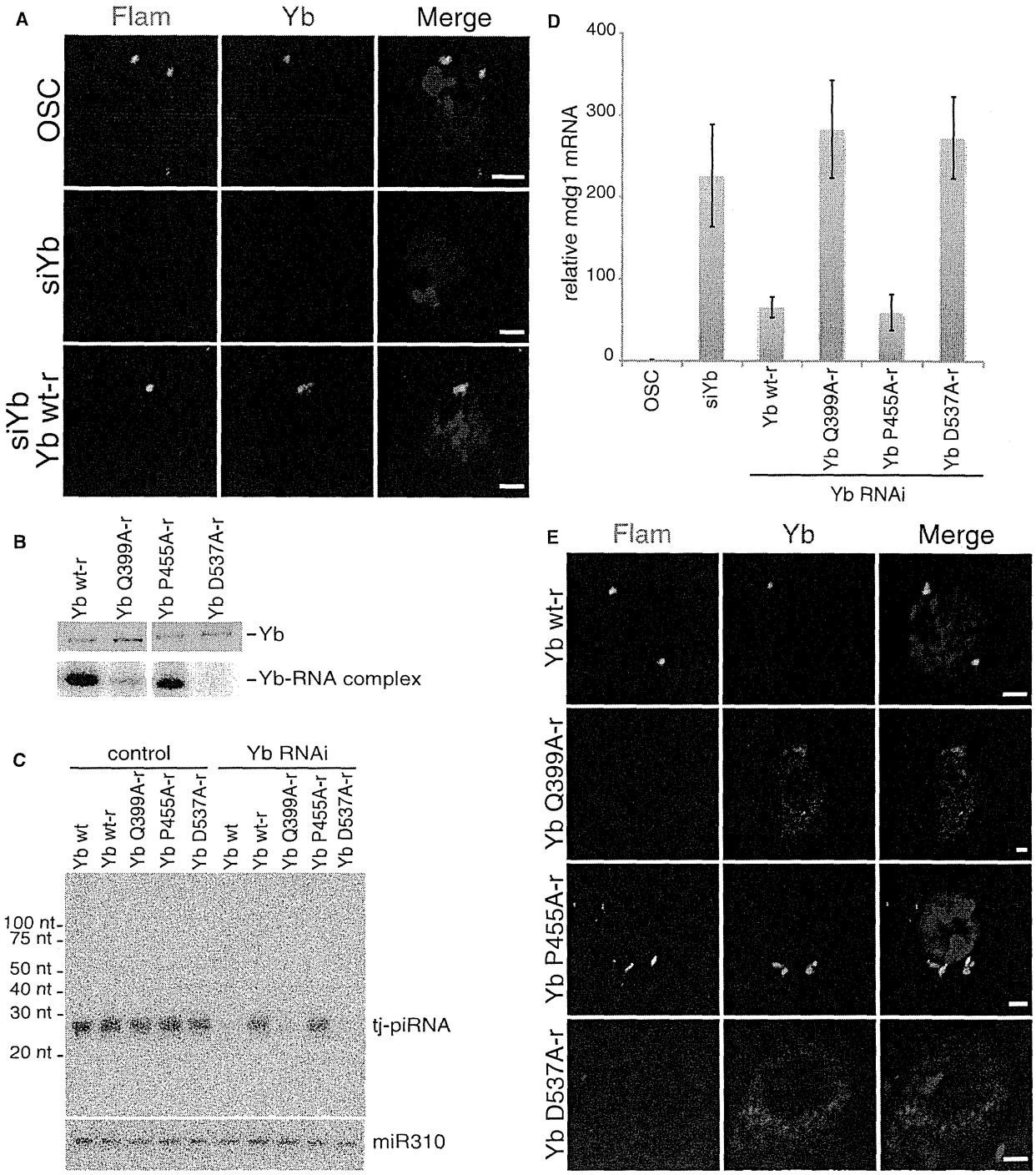

Figure 3. Yb Requirement for Flam Body and Yb Body Formation

(A) Depletion of Yb in OSCs abolishes formation of Flam bodies (green) and Yb bodies (magenta). Expression of siRNA-resistant Yb (Yb WT-r) restored the formation of both structures. Nuclei are stained with DAPI (blue). Scale bar, 2 μm.

(B) The RNA-binding activity of Yb is abolished by either the Q399A or the D537A mutation in the Yb NTD. Western blotting using the anti-Yb antibody shows that an approximately equal amount of Yb was obtained through Yb-CLIP (top). However, the intensity of the Yb Q399A- and D537A-RNA complexes was much lower than that of the Yb P455A- and Yb WT-r-RNA complexes (bottom).

(legend continued on next page)

shown). These observations support the notion that Yb is the central player in piRNA biogenesis in OSCs; namely, Yb triggers the fabrication of two perinuclear structures, Yb bodies and Flam bodies, the hubs for piRNA maturation and piRNA intermediate concentration, respectively, in the piRNA pathway.

RNA Binding of Yb through the N-Terminal RecA-like Domain Is Required for Yb Body and Flam Body Formation

Yb shows significant similarity to DEAD-box RNA helicases such as Vasa in *Drosophila* and DDH5 and DDX18 in humans, especially in the N-terminal RecA-like domain (NTD) consisting of a Q motif and motifs I, Ia, Ib, II, and III (Figure S3D). To examine the functional involvement of the NTD of Yb in the piRNA pathway, we individually mutated highly conserved residues in Yb, Gln399, Pro455, and Asp537, to Ala. Gln399, Pro455, and Asp537 reside within the Q motif, motif Ia, and motif II, respectively (Figure S3D). In Vasa, Gln272 in the Q motif and Asp399 in motif II, which correspond to Gln399 and Asp537 in Yb, are involved in ATP binding, while Pro326 in motif Ia, which corresponds to Yb-Pro455, contributes to RNA substrate binding (Sengoku et al., 2006). ATP binding by Vasa is necessary for RNA binding (Banroques et al., 2010). Thus, we expected that the alteration of Gln399, Pro455, and Asp537 in Yb to Ala would abolish the RNA-binding function of Yb. Indeed, crosslinking and immunoprecipitation (CLIP) showed that mutation of Gln399 and Asp537 to Ala (Q399A and D537A, respectively) severely decreased the RNA-binding activity of Yb (Figure 3B). Thus, Yb is a bona fide RNA-binding protein and binds RNA substrates through the conserved NTD.

To determine if the RNA-binding activity of Yb is required in the piRNA pathway, three mutants of siRNA-resistant Yb (Q399A, P455A, and D537A), as well as Yb WT, were expressed in Yb-depleted OSCs (Figure S3E). Northern blotting showed that while the WT control Yb WT-r rescued the defect in piRNA accumulation caused by loss of Yb function, the Q399A and D537A mutants (Q399A-r and D537A-r) failed to rescue the defective phenotype (Figure 3C). The P455A mutant (P455A-r) behaved similarly to the WT control (Figure 3C), suggesting that Pro455, despite its high conservation (Figure S3D), is dispensable for piRNA biogenesis. We also examined the expression level of the *mdg1* transposon in the transfected cells, and found that Yb WT-r and P455A-r rerepressed *mdg1*, but Q399A-r and D537A-r failed to do so (Figure 3D). Q399 and D537, but not P455, in the Yb NTD are necessary for both piRNA production and piRNA-mediated transposon silencing.

We then asked if Yb WT-r and the three Yb mutants in Yb-depleted OSCs were able to restore formation of Flam bodies and Yb bodies. Yb WT-r and P455A-r were able to form Yb bodies, while Q399A-r and D537A-r were dispersed in the cytosol and did not accumulate at specific foci (Figures 3E and S3F). Correlating with this, Flam bodies appeared when Yb WT-r and P455A-r were expressed (Figures 3E and S3F). However, the expression of Q399A-r and D537A-r did not result in the formation of Flam bodies (Figures 3E and S3F). Quantitative RT-PCR (qRT-PCR) detected *flam*-piRNA intermediates in Q399A-r- and D537A-r-expressing OSCs, where endogenous Yb had been depleted by RNAi (Figure S3G). Thus, the substitution of endogenous Yb with Q399-r or D537A-r mutant did not interfere with *flam* expression.

Yb Directly Binds *flam*-piRNA Intermediates, but Not Neighboring Protein-Coding *DIP1* Transcripts

Does endogenous Yb in OSCs indeed bind *flam* transcripts that serve as piRNA intermediates in piRNA biogenesis? To address this question, HITS-CLIP was performed in OSCs using an anti-Yb antibody. Illumina HiSeq2000 sequencing resulted in a total of 72,464,026 reads, consisting of 353,894 unique reads. We mapped these unique reads to the *Drosophila* genome, and 220,197 reads (62.2%) were mapped to a unique position. Annotation of mapped Yb-CLIP tags was similar to that of Piwi-associated piRNAs (Saito et al., 2009); over half of the reads (50.3%) were mapped to transposon regions (Figure S4A).

Further analysis of the Yb-CLIP tags showed that Yb most preferably binds transcripts from the *flam* locus among all piRNA clusters (Figure S4B). We then precisely analyzed the Yb-CLIP tags mapped to the *flam* locus. The distribution of the Yb-CLIP tags on the *flam* locus revealed that Yb in OSCs indeed associates with *flam* transcripts (Figure 4A). The Yb-CLIP tags significantly overlapped with *flam*-piRNAs associated with Piwi in OSCs (Figure 4A). By contrast, none of the Yb-CLIP tags were mapped to a neighboring coding gene, *DIP1* (Figures 4A and 4B), which is highly expressed in OSCs (Sienski et al., 2012; Cherbas et al., 2011). Yb-CLIP tag mapping to protein-coding genes that produce genic piRNAs (Saito et al., 2009) revealed that Yb almost exclusively binds the 3′ UTR, but not the protein coding sequence (CDS) or 5′ UTR of the transcripts (Figure S4C). The 3′ UTR, but not the CDS or the 5′ UTR, of genic piRNA-producing mRNAs serves as the piRNA sources (Robine et al., 2009; Saito et al., 2009). These results suggest that Yb directly, and somewhat selectively, binds piRNA intermediates in OSCs.

DISCUSSION

In this study, we visualized *flam*-piRNA intermediates in OSCs and follicle cells using RNA-FISH and EM-ISH and revealed that they concentrate at perinuclear Flam bodies. Flam bodies locate in very close proximity to Yb bodies, the sites of piRNA maturation and piRISC formation. We postulated that *flam* signals might also be detectable within Yb bodies. However, this was not the case (Figures 1B and S1A). The simplest explanation for this observation is that piRNA processing at Yb bodies occurs so quickly, and the processed piRNAs localize to the nucleus as

(C) Expression of Yb WT-r and P455A-r, but not Q399A-r and D537A-r, rescued the defect in piRNA accumulation in Yb-depleted OSCs. A piRNA arising from a *traffic jam* (*tj*) gene (Saito et al., 2009) was visualized by northern blotting using a specific DNA probe. miR310, loading control.

(D) Expression of Yb WT-r and P455A-r rerepressed the *mdg1* transposon in Yb-depleted OSCs, but expression of Q399A-r or D537A-r could not.

(E) Mutation of Q399A and D537A in Yb abolished Flam body (green) and Yb body (magenta) formation in OSCs. Endogenous Yb was depleted by RNAi. Nuclei are stained with DAPI (blue). Scale bar, 2 μm.

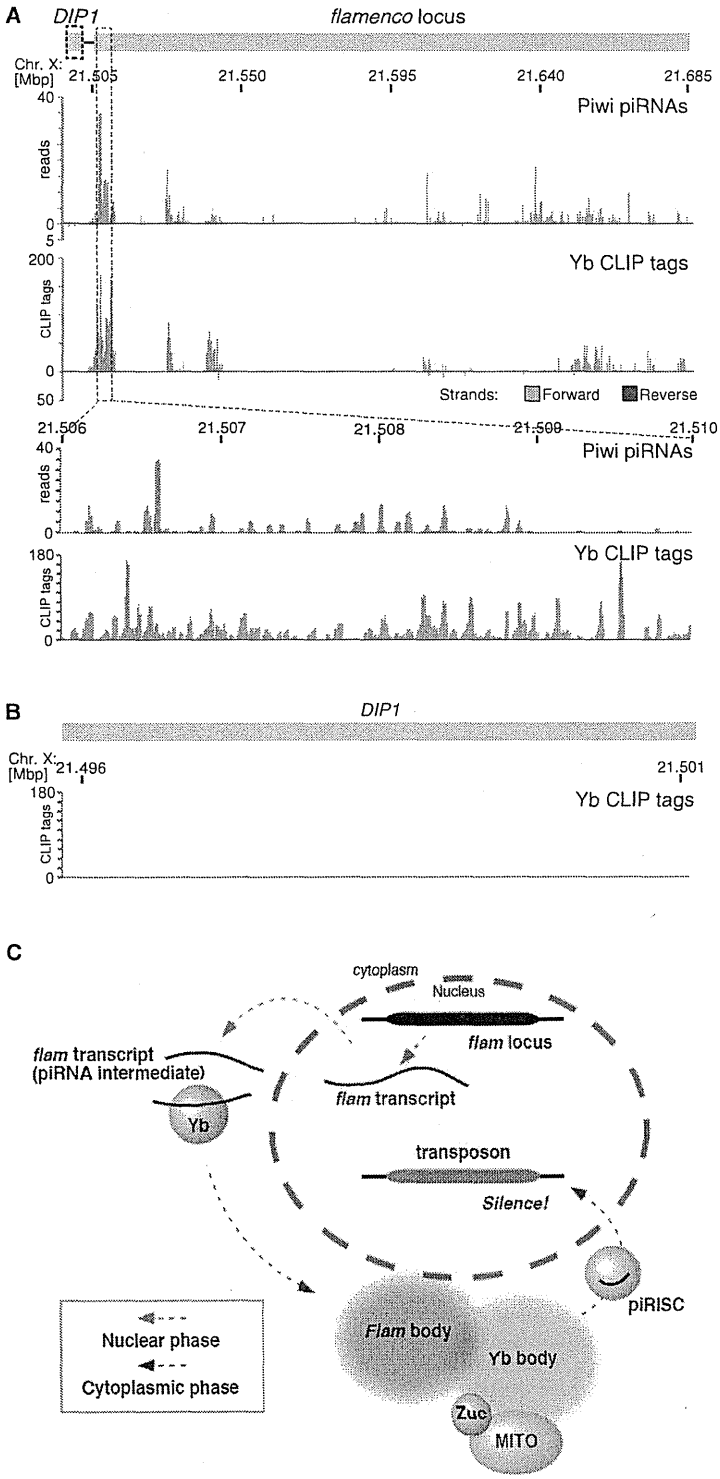

Figure 4. Yb Binds *flam* Transcripts, but Not *DIP1* mRNAs, In Vivo

(A) Mapped Piwi-piRNA reads and Yb-CLIP tags on the *DIP1* coding and *flam* cluster region. Forward reads are shown in blue, and reverse reads are shown in red. The number on the side of tracks denotes the number of reads in each position. Genomic coordinates are marked above the tracks. The bottom panel shows a further zoom-in view of sequences around the region where the RNA-FISH probe was designed to bind.

(B) A further zoom-in view of sequences of the *DIP1* gene in (A) (boxed by a dotted blue line).

(C) A new model for primary piRNA biogenesis in OSCs. The transcription and nuclear export of the transcripts are considered to be the "nuclear phase" of piRNA biogenesis. The *flam* transcripts become *flam*-piRNA intermediates by "shortening" in either the nucleus or the cytoplasm. The mechanism underlying the shortening process remains unknown. Yb binds piRNA intermediates in the cytoplasm and locates to Flam bodies. piRNA intermediates are further processed to mature piRNAs at Yb bodies with the help of Zuc on mitochondria (MITO) and loaded onto Piwi, giving rise to the piRISC. The piRISC is imported to the nucleus, where the RNP complex exerts its function: transcriptional silencing of transposons. Yb-piRNA intermediate association, piRNA maturation, and piRISC assembly are considered to be the "cytoplasmic phase" of piRNA biogenesis. Components of Yb bodies include Yb, Armi, Vret, SoYb, and Shu, all of which are required for piRNA biogenesis and piRISC formation in OSCs.

piRISCs so immediately, that the *flam* signal at Yb bodies was below the level of detection at Yb bodies.

In Zuc-depleted cells, *flam* transcripts were detected predominantly as *flam*-piRNA intermediates, being several hundred to 4,000 nt in length (Figures 2C and S2A), while the full transcriptional unit of *flam* is estimated to be over 180 kb (Brennecke et al., 2007; Malone et al., 2009). Both Yb body and Flam body formation require Yb, or more precisely, its RNA-binding activity through its NTD (Figures 3B, 3E, and S3F). Yb binds *flam*-piRNA intermediates directly (Figure 4A). Based on these findings, we propose a new model for primary piRNA biogenesis in ovarian soma (Figure 4C), in which the association of Yb with piRNA intermediates, which most likely occurs in the cytoplasm because Yb is a cytoplasmic protein (Olivieri et al., 2010; Saito et al., 2010), is the initiation point of the cytoplasmic phase of piRNA biogenesis. This follows the nuclear phase of piRNA biogenesis: *flam* transcription and nuclear export of *flam* transcripts through the nuclear pores. *flam* transcription is initiated by RNA polymerase II and requires the transcriptional factor Cubitus interruptus (Goriaux et al., 2014). However, it is not known by which export factors and in what lengths the *flam* transcripts are exported from the nucleus. Further investigation will be required for a detailed understanding of the nuclear phase of piRNA biogenesis.

The locations of the genomic *flam* loci in the nucleus and Flam bodies do not seem to be arranged to be close to each other, meaning that the *flam* transcripts move a long distance to arrive at Flam bodies (Figure 4C). Do the *flam* transcripts move within the nucleus to get closer to Flam bodies before export to the cytoplasm? Alternatively, does nuclear export occur first and then *flam* transcripts are localized to Flam bodies? Yb localization in the cytoplasm seems to be so dynamic that a point mutation in Yb that disrupts the RNA-binding capacity of Yb drastically changes the subcellular localization of Yb, causing it to be scattered evenly in the cytosol (Figures 3E and S3F). Thus, the latter scenario appears more likely, in which Yb plays a crucial role; upon nuclear export, Yb captures *flam* transcripts through direct binding and localizes them, as *flam*-piRNA intermediates, to Flam bodies. Flam body formation depends on the RNA-binding activity of Yb, a cytoplasmic protein (Olivieri et al., 2010; Saito et al., 2010); this notion further supports the idea that Flam bodies are cytoplasmic structures.

Unlike *flam* transcripts, *DIP1* mRNAs were virtually undetectable in Yb-CLIP tags (Figures 4A and 4B), although the *DIP1* protein-coding gene and the *flam* piRNA cluster are neighbors on chromosome X (Figure 1A) and *DIP1* is expressed in OSCs. We looked carefully at the sequences of Yb-CLIP tags but found no obvious consensus sequences. Yb may recognize binding substrates owing to higher-order structures.

Immunoelectron microscopy using an anti-Yb antibody showed that Yb bodies are often attached to mitochondria, to which Zuc endoribonuclease, the piRNA intermediate processor, anchors on the surface to face into cytoplasmic Yb bodies (Figure 1D). This peculiar spatial arrangement of Zuc and Yb bodies, along with Flam bodies, integrates all the ingredients necessary for primary piRNA production locally, enhancing the rates of piRISC assembly. Another virtue of this perinuclear arrangement is that it enables assembled piRISCs to be immediately imported into the nucleus, where the RNP complex (i.e., the PIWI-piRNA complex) exerts its nuclear-specific function of silencing transposon transcription (Sienski et al., 2012). How does Yb decide where within the perinuclear region to integrate all the materials necessary for primary piRNA biogenesis? Reconstitution of the whole machinery in, for instance, nongonadal somatic Schneider2 cells, in which no primary piRNAs are otherwise expressed, might address this fundamental question.

EXPERIMENTAL PROCEDURES

Detailed procedures are provided in Supplemental Experimental Procedures.

Drosophila Strains

Yellow white (*y w*) and the *flam [KG00476]* and the *fs(1)Yb[72]* alleles were used. Fly stocks were maintained at 25°C.

Cell Culture and RNAi

OSCs were grown in OSC medium prepared from Shields and Sang M3 Insect Medium (Sigma) supplemented with 0.6 mg/ml glutathione, 10% fetal bovine serum, 10 mU/ml insulin, and 10% fly extract. RNAi was performed using RNA oligos shown in Table S1.

Production of Anti-Yb Antibodies

Monoclonal antibodies against Yb were raised primarily as described previously (Ohtani et al., 2013). A recombinant protein consisting of glutathione S-transferase and the N-terminal region of Yb (200 amino acids) was purified from *E. coli* and injected into mice.

RNA-FISH

The fluorescein isothiocyanate (FITC)- and digoxigenin-labeled RNA probes were prepared using RNA labeling mixture (Roche) and SP6RNA polymerase (Roche) according to the manufacturer's instructions. To prepare a probe specific for the *flam* locus, OSC genomic DNA was used as a template for PCR. The primers used for PCR are indicated in Table S1. In situ hybridization was carried out essentially as described previously (Sone et al., 2007).

DNA-FISH

Digoxigenin- or biotin-labeled DNA probes were prepared using Nick Translation Mix (Roche) according to the manufacturer's instructions. To prepare the probes, bacterial artificial chromosome clones DME1-021J16 (upstream of the *flam* locus) and DME1-014M21 (downstream of the *flam* locus), were used as templates. OSCs were treated with ice-cold 0.75 M KCl for 5 min and then, after resuspending in acetic acid-methanol (1:3), spread onto slides. The slides were treated essentially according to the procedures of Masumoto et al. (Masumoto et al., 1989).

Immunofluorescence

Immunofluorescence was performed primarily as described previously (Ohtani et al., 2013; Saito et al., 2009).

Body Counting

Confocal images of immunofluorescence were transferred to the Columbus System (PerkinElmer Japan) and analyzed by Building Block (PerkinElmer Japan). Nuclei were masked and then perinuclear signals for Yb bodies and Flam bodies were detected.

Electron Microscopy In Situ Hybridization

OSCs were fixed with 4% paraformaldehyde (PFA) in 0.1 M PBS (pH 7.4) overnight and then washed with RNase-free PBS. The samples were hybridized with FITC-conjugated specific RNA probe, except that 0.5% Triton X-100 was used for 5 min. Samples were incubated with a primary rabbit anti-FITC (1:500) antibody and then washed in 0.1 M phosphate buffer (PB) containing

0.005% saponin. Samples were incubated for 24 hr at 4°C with nanogold-conjugated anti-rabbit secondary antibody (1:100, Invitrogen).

Immunoelectron Microscopy

OSCs were fixed with 0.1% glutaraldehyde and 4% PFA in 0.1 M PBS, followed by incubation with 5% Block Ace containing 0.1% saponin in 0.1 M PB. The cells were stained with anti-Yb antibody (1:250) and nanogold-conjugated anti-mouse secondary antibody (1:100, Invitrogen).

Western Blot Analysis

Western blotting was performed primarily as described previously (Miyoshi et al., 2005).

Northern Blot Analysis

For *flam* transcript detection, total RNAs were isolated from OSC using ISOGEN (Nippon Gene). Hybridization was performed with random-labeled antisense oligodeoxynucleotide probe. Small RNAs were detected essentially as previously described (Saito et al., 2009).

Plasmid Construction

An expression vector for myc-Yb WT was generated by inserting the WT Yb coding region into the pAcM vector (Saito et al., 2009). myc-Yb-r was constructed as essentially described previously (Saito et al., 2010). Primers are listed in Table S1.

qRT-PCR Analysis

Reverse transcription was performed using a PrimerScript RT Master Mix (TaKaRa). The resulting cDNAs were amplified using a LightCycler 480 Real-Time PCR Instrument II (Roche) with SYBR Premix Ex Taq (TaKaRa). The primers used are listed in Table S1.

CLIP

CLIP was performed primarily as described previously (Jaskiewicz et al., 2012). Anti-Yb was used to immunopurify Yb from OSCs after irradiation by UV (254 nm) for crosslinking.

Bioinformatic Analysis

The Yb-CLIP library was sequenced using the Illumina HiSeq2000 platform according to the manufacturer's instructions. The average base-wise quality was checked, and those that passed quality control were subjected to analyses.

ACCESSION NUMBERS

Yb-CLIP tag sequencing data have been deposited in the Gene Expression Omnibus under the accession number GSE54875.

SUPPLEMENTAL INFORMATION

Supplemental Information includes Supplemental Experimental Procedures, four figures, and one table and can be found with this article online at http://dx.doi.org/10.1016/j.celrep.2014.05.043.

AUTHOR CONTRIBUTIONS

M.Y., H.I., S.N., Y.W.I., S.S., M.K.K., and K.S. designed and performed experiments and helped write the manuscript. H.O. supervised electron microscopic experiments. H.S. and M.C.S. conceived the study and wrote the manuscript.

ACKNOWLEDGMENTS

We thank H. Masumoto for technical advice and Y. Iyoda, H. Kotani, T. Yano, and T. Nagai for technical assistance. We also thank M. Isogai and M. Shimura (PerkinElmer Japan) for their assistance with fluorescence quantification. This work was supported by CREST-JST (to M.C.S.), by a Grant-in-Aid for Scientific Research from MEXT (to S.N., Y.W.I., S.S., K.S., H.O., H.S. and M.C.S.), and by a Grant-in-Aid for the Global COE program from MEXT to Keio University (H.S. and H.O.).

Received: December 16, 2013
Revised: April 9, 2014
Accepted: May 21, 2014
Published: June 19, 2014

REFERENCES

Aravin, A.A., Hannon, G.J., and Brennecke, J. (2007). The Piwi-piRNA pathway provides an adaptive defense in the transposon arms race. Science *318*, 761–764.

Banroques, J., Doère, M., Dreyfus, M., Linder, P., and Tanner, N.K. (2010). Motif III in superfamily 2 "helicases" helps convert the binding energy of ATP into a high-affinity RNA binding site in the yeast DEAD-box protein Ded1. J. Mol. Biol. *396*, 949–966.

Brennecke, J., Aravin, A.A., Stark, A., Dus, M., Kellis, M., Sachidanandam, R., and Hannon, G.J. (2007). Discrete small RNA-generating loci as master regulators of transposon activity in *Drosophila*. Cell *128*, 1089–1103.

Cherbas, L., Willingham, A., Zhang, D., Yang, L., Zou, Y., Eads, B.D., Carlson, J.W., Landolin, J.M., Kapranov, P., Dumais, J., et al. (2011). The transcriptional diversity of 25 *Drosophila* cell lines. Genome Res. *21*, 301–314.

Choi, S.Y., Huang, P., Jenkins, G.M., Chan, D.C., Schiller, J., and Frohman, M.A. (2006). A common lipid links Mfn-mediated mitochondrial fusion and SNARE-regulated exocytosis. Nat. Cell Biol. *8*, 1255–1262.

Cook, H.A., Koppetsch, B.S., Wu, J., and Theurkauf, W.E. (2004). The *Drosophila* SDE3 homolog armitage is required for oskar mRNA silencing and embryonic axis specification. Cell *116*, 817–829.

Dennis, C., Zanni, V., Brasset, E., Eymery, A., Zhang, L., Mteirek, R., Jensen, S., Rong, Y.S., and Vaury, C. (2013). "Dot COM", a nuclear transit center for the primary piRNA pathway in *Drosophila*. PLoS ONE *8*, e72752.

Dönertas, D., Sienski, G., and Brennecke, J. (2013). Drosophila Gtsf1 is an essential component of the Piwi-mediated transcriptional silencing complex. Genes Dev. *27*, 1693–1705.

Goriaux, C., Desset, S., Renaud, Y., Vaury, C., and Brasset, E. (2014). Transcriptional properties and splicing of the *flamenco* piRNA cluster. EMBO Rep. *15*, 411–418.

Gunawardane, L.S., Saito, K., Nishida, K.M., Miyoshi, K., Kawamura, Y., Nagami, T., Siomi, H., and Siomi, M.C. (2007). A slicer-mediated mechanism for repeat-associated siRNA 5′ end formation in *Drosophila*. Science *315*, 1587–1590.

Haase, A.D., Fenoglio, S., Muerdter, F., Guzzardo, P.M., Czech, B., Pappin, D.J., Chen, C., Gordon, A., and Hannon, G.J. (2010). Probing the initiation and effector phases of the somatic piRNA pathway in *Drosophila*. Genes Dev. *24*, 2499–2504.

Handler, D., Olivieri, D., Novatchkova, M., Gruber, F.S., Meixner, K., Mechtler, K., Stark, A., Sachidanandam, R., and Brennecke, J. (2011). A systematic analysis of *Drosophila* TUDOR domain-containing proteins identifies Vreteno and the Tdrd12 family as essential primary piRNA pathway factors. EMBO J. *30*, 3977–3993.

Ipsaro, J.J., Haase, A.D., Knott, S.R., Joshua-Tor, L., and Hannon, G.J. (2012). The structural biochemistry of Zucchini implicates it as a nuclease in piRNA biogenesis. Nature *491*, 279–283.

Ishizu, H., Siomi, H., and Siomi, M.C. (2012). Biology of PIWI-interacting RNAs: new insights into biogenesis and function inside and outside of germlines. Genes Dev. *26*, 2361–2373.

Jaskiewicz, L., Bilen, B., Hausser, J., and Zavolan, M. (2012). Argonaute CLIP—a method to identify *in vivo* targets of miRNAs. Methods *58*, 106–112.

Juliano, C., Wang, J., and Lin, H. (2011). Uniting germline and stem cells: the function of Piwi proteins and the piRNA pathway in diverse organisms. Annu. Rev. Genet. *45*, 447–469.

Khurana, J.S., and Theurkauf, W. (2010). piRNAs, transposon silencing, and *Drosophila* germline development. J. Cell Biol. *191*, 905–913.

Malone, C.D., Brennecke, J., Dus, M., Stark, A., McCombie, W.R., Sachidanandam, R., and Hannon, G.J. (2009). Specialized piRNA pathways act in germline and somatic tissues of the *Drosophila* ovary. Cell *137*, 522–535.

Masumoto, H., Sugimoto, K., and Okazaki, T. (1989). Alphoid satellite DNA is tightly associated with centromere antigens in human chromosomes throughout the cell cycle. Exp. Cell Res. *181*, 181–196.

Mével-Ninio, M., Pelisson, A., Kinder, J., Campos, A.R., and Bucheton, A. (2007). The *flamenco* locus controls the gypsy and ZAM retroviruses and is required for *Drosophila* oogenesis. Genetics *175*, 1615–1624.

Miyoshi, K., Tsukumo, H., Nagami, T., Siomi, H., and Siomi, M.C. (2005). Slicer function of *Drosophila* Argonautes and its involvement in RISC formation. Genes Dev. *19*, 2837–2848.

Muerdter, F., Guzzardo, P.M., Gillis, J., Luo, Y., Yu, Y., Chen, C., Fekete, R., and Hannon, G.J. (2013). A genome-wide RNAi screen draws a genetic framework for transposon control and primary piRNA biogenesis in *Drosophila*. Mol. Cell *50*, 736–748.

Nishimasu, H., Ishizu, H., Saito, K., Fukuhara, S., Kamatani, M.K., Bonnefond, L., Matsumoto, N., Nishizawa, T., Nakanaga, K., Aoki, J., et al. (2012). Structure and function of Zucchini endoribonuclease in piRNA biogenesis. Nature *491*, 284–287.

Ohtani, H., Iwasaki, Y.W., Shibuya, A., Siomi, H., Siomi, M.C., and Saito, K. (2013). DmGTSF1 is necessary for Piwi-piRISC-mediated transcriptional transposon silencing in the *Drosophila* ovary. Genes Dev. *27*, 1656–1661.

Olivieri, D., Sykora, M.M., Sachidanandam, R., Mechtler, K., and Brennecke, J. (2010). An in vivo RNAi assay identifies major genetic and cellular requirements for primary piRNA biogenesis in *Drosophila*. EMBO J. *29*, 3301–3317.

Olivieri, D., Senti, K.A., Subramanian, S., Sachidanandam, R., and Brennecke, J. (2012). The cochaperone shutdown defines a group of biogenesis factors essential for all piRNA populations in *Drosophila*. Mol. Cell *47*, 954–969.

Pillai, R.S., and Chuma, S. (2012). piRNAs and their involvement in male germline development in mice. Dev. Growth Differ. *54*, 78–92.

Qi, H., Watanabe, T., Ku, H.Y., Liu, N., Zhong, M., and Lin, H. (2011). The Yb body, a major site for Piwi-associated RNA biogenesis and a gateway for Piwi expression and transport to the nucleus in somatic cells. J. Biol. Chem. *286*, 3789–3797.

Robine, N., Lau, N.C., Balla, S., Jin, Z., Okamura, K., Kuramochi-Miyagawa, S., Blower, M.D., and Lai, E.C. (2009). A broadly conserved pathway generates 3'UTR-directed primary piRNAs. Curr. Biol. *19*, 2066–2076.

Saito, K., Inagaki, S., Mituyama, T., Kawamura, Y., Ono, Y., Sakota, E., Kotani, H., Asai, K., Siomi, H., and Siomi, M.C. (2009). A regulatory circuit for *piwi* by the large Maf gene *traffic jam* in *Drosophila*. Nature *461*, 1296–1299.

Saito, K., Ishizu, H., Komai, M., Kotani, H., Kawamura, Y., Nishida, K.M., Siomi, H., and Siomi, M.C. (2010). Roles for the Yb body components Armitage and Yb in primary piRNA biogenesis in *Drosophila*. Genes Dev. *24*, 2493–2498.

Sengoku, T., Nureki, O., Nakamura, A., Kobayashi, S., and Yokoyama, S. (2006). Structural basis for RNA unwinding by the DEAD-box protein *Drosophila* Vasa. Cell *125*, 287–300.

Sienski, G., Dönertas, D., and Brennecke, J. (2012). Transcriptional silencing of transposons by Piwi and maelstrom and its impact on chromatin state and gene expression. Cell *151*, 964–980.

Siomi, M.C., Sato, K., Pezic, D., and Aravin, A.A. (2011). PIWI-interacting small RNAs: the vanguard of genome defence. Nat. Rev. Mol. Cell Biol. *12*, 246–258.

Sone, M., Hayashi, T., Tarui, H., Agata, K., Takeichi, M., and Nakagawa, S. (2007). The mRNA-like noncoding RNA Gomafu constitutes a novel nuclear domain in a subset of neurons. J. Cell Sci. *120*, 2498–2506.

Szakmary, A., Reedy, M., Qi, H., and Lin, H. (2009). The Yb protein defines a novel organelle and regulates male germline stem cell self-renewal in *Drosophila melanogaster*. J. Cell Biol. *185*, 613–627.

Zamparini, A.L., Davis, M.Y., Malone, C.D., Vieira, E., Zavadil, J., Sachidanandam, R., Hannon, G.J., and Lehmann, R. (2011). Vreteno, a gonad-specific protein, is essential for germline development and primary piRNA biogenesis in *Drosophila*. Development *138*, 4039–4050.

Stem Cell Reports
Article

ISSCR

OPEN ACCESS

Involvement of ER Stress in Dysmyelination of Pelizaeus-Merzbacher Disease with *PLP1* Missense Mutations Shown by iPSC-Derived Oligodendrocytes

Yuko Numasawa-Kuroiwa,[1,2] Yohei Okada,[1,3,*] Shinsuke Shibata,[1] Noriyuki Kishi,[1] Wado Akamatsu,[1] Masanobu Shoji,[4] Atsushi Nakanishi,[4] Manabu Oyama,[5] Hitoshi Osaka,[6] Ken Inoue,[7] Kazutoshi Takahashi,[8] Shinya Yamanaka,[8] Kenjiro Kosaki,[9] Takao Takahashi,[2] and Hideyuki Okano[1,*]

[1]Department of Physiology, School of Medicine, Keio University, 35 Shinanomachi, Shinjuku-ku, Tokyo 160-8582, Japan
[2]Department of Pediatrics, School of Medicine, Keio University, 35 Shinanomachi, Shinjuku-ku, Tokyo 160-8582, Japan
[3]Department of Neurology, School of Medicine, Aichi Medical University, 1-1 Yazako Karimata, Nagakute, Aichi 480-1195, Japan
[4]Advanced Science Research Laboratories, Takeda Pharmaceutical Company Limited, 26-1 Muraoka-Higashi 2-Chome, Fujisawa, Kanagawa 251-8555, Japan
[5]Department of Dermatology, School of Medicine, Keio University, 35 Shinanomachi, Shinjuku-ku, Tokyo 160-8582, Japan
[6]Department of Pediatrics, Jichi Medical School, 3311-1 Yakushiji, Shimotsuke-shi, Tochigi 329-0498, Japan
[7]Department of Mental Retardation and Birth Defect Research, National Institute of Neuroscience, National Center of Neurology and Psychiatry, 4-1-1 Ogawahigashi-machi, Kodaira-shi, Tokyo 187-8551, Japan
[8]Center for Induced Pluripotent Stem Cell Research and Application, Graduate School of Medicine, Institute for Frontier Medical Sciences, Kyoto University, Kyoto 606-8507, Japan
[9]Center for Medical Genetics, School of Medicine, Keio University, 35 Shinanomachi, Shinjuku-ku, Tokyo 160-8582, Japan
*Correspondence: yohei@a6.keio.jp (Y.O.), hidokano@a2.keio.jp (H.O.)
http://dx.doi.org/10.1016/j.stemcr.2014.03.007

SUMMARY

Pelizaeus-Merzbacher disease (PMD) is a form of X-linked leukodystrophy caused by mutations in the *proteolipid protein 1* (*PLP1*) gene. Although PLP1 proteins with missense mutations have been shown to accumulate in the rough endoplasmic reticulum (ER) in disease model animals and cell lines transfected with mutant *PLP1* genes, the exact pathogenetic mechanism of PMD has not previously been clarified. In this study, we established induced pluripotent stem cells (iPSCs) from two PMD patients carrying missense mutation and differentiated them into oligodendrocytes in vitro. In the PMD iPSC-derived oligodendrocytes, mislocalization of mutant PLP1 proteins to the ER and an association between increased susceptibility to ER stress and increased numbers of apoptotic oligodendrocytes were observed. Moreover, electron microscopic analysis demonstrated drastically reduced myelin formation accompanied by abnormal ER morphology. Thus, this study demonstrates the involvement of ER stress in pathogenic dysmyelination in the oligodendrocytes of PMD patients with the *PLP1* missense mutation.

INTRODUCTION

Analysis of differentiated cells from disease-specific, human induced pluripotent stem cells (iPSCs) enables the construction of pathological models using the patients' own cells. Such analyses are particularly useful for the study of neurodegenerative disorders because it is difficult to collect brain-tissue samples from these patients.

Pelizaeus-Merzbacher disease (PMD) is a dysmyelinating disorder of the CNS that is usually observed during childhood. PMD is classified into two subtypes: the classical and connatal forms. In the classical form, patients usually show a delay in psychomotor development within the first year of life but exhibit relatively slow disease progression over the first decade. In contrast, in the connatal form, patients generally show arrested congenital psychomotor development and exhibit a progressive disease course with severe neurological impairment. The degree of dysmyelination has been shown to correlate well with the clinical severity of PMD (Seitelberger, 1995). The *proteolipid protein 1* (*PLP1*) gene has been identified as a causative gene for PMD. PLP1 is a transmembrane protein that is abundantly expressed in compact myelin in oligodendrocytes (OLs) and plays a structural role in the formation and maintenance of myelin sheaths (Gow et al., 1997; Mikoshiba et al., 1991). Three distinct types of *PLP1* mutation have been reported to date: point mutations, duplications, and deletions. Missense mutations in the *PLP1* gene account for 30% of the genetic abnormalities found in PMD patients and are responsible for most of connatal cases. Based on analyses using cell lines transfected with mutant *PLP1* genes (Gow and Lazzarini, 1996) or a mouse model of PMD (the *msd* mouse; Gow et al., 1998), the underlying pathogenesis in most patients with missense mutations is thought to involve the accumulation of misfolded mutant PLP1 proteins in the rough endoplasmic reticulum (ER) (Southwood et al., 2002) and the induction of ER stress, resulting in activation of the unfolded protein response (UPR). Although UPR attenuates general translation to reduce the protein load into ER and increase expression of chaperone proteins to facilitate protein folding, excessive levels of unfolded proteins have been shown to activate apoptotic pathway of UPR to eliminate damaged OLs.

However, despite the precise analyses conducted using conventional cellular and animal PMD models, it has not been possible to examine the actual correlation between the known molecular pathogenesis and cell biological phenotypes, including abnormalities in OL differentiation, myelination, and cell death. In addition, those previous results were obtained through analyses using nonhuman models, non-patient-derived cells, or nonoligodendrocyte models, and it is unknown whether the results obtained in those models are applicable to human patients. Although the establishment of iPSCs from a PMD patient with partial duplication of *PLP1* gene has been reported, those iPSCs were not differentiated into oligodendrocytes for disease modeling (Shimojima et al., 2012). Thus, in the present study, we focused on the pathologic effects of *PLP1* missense mutations and established patient-specific iPSCs from two PMD patients with different mutation sites and different levels of clinical severity.

We differentiated the iPSCs into OL lineage cells and examined the pathogenic changes in the PMD iPSC-derived OLs. We confirmed the accumulation and mislocalization of mutant PLP1 proteins to the ER, a high level of stress susceptibility, and increased apoptosis in PMD iPSC-derived OLs. In addition, through transmission electron microscopic analysis, we verified decreases in the frequency of myelin formation and the thickness of the myelin sheath compared with control cells. More importantly, we also demonstrated that these pathogenic changes observed in iPSC-derived OLs were consistent with the different levels of clinical severity between the two PMD patients. Thus, this report describes the modeling of human PMD with *PLP1* missense mutations using patient-specific, iPSC-derived OLs. These results have demonstrated the usefulness of iPSC-derived OLs for the analysis of the pathogenic processes in human dysmyelinating neurological disorders.

RESULTS

Clinical Features of PMD Patients

We established iPSCs from two patients with point mutations in the transmembrane domain (patient 1: PMD1) and extracellular domain (patient 2: PMD2) of the *PLP1* gene (Figure 1C). PMD1 was a 1-year-old male with the connatal form of PMD. He was diagnosed with PMD at the age of 4 months, when he was found to exhibit poor head control and nystagmus and was unable to follow objects. He showed poor feeding and was fed through a gastrostomy tube from the age of 21 months. Psychomotor development was not observed, even at the age of 5 years. MRI of the patient's brain revealed mild and diffuse atrophy, dilatation of the ventricles, and diffuse high-intensity signals in the white matter of the cerebrum and brainstem in a T2-weighted image (T2WI) (Figure 1A). A direct sequencing analysis of genomic DNA from the patient's leukocytes showed a novel missense mutation, c.757 T > A (p.Ser253Thr), in exon 6 of the *PLP1* gene (Figure 1B). This amino acid change has not been previously reported, but different type of mutation at this same site, Ser253Phe, has been reported in other patients with the connatal form of PMD (Hodes et al., 1998). This change was not identified in more than 200 normal individuals; thus, it was considered to be a causative mutation for PMD.

Patient 2 (PMD2) was a 20-year-old male with the classical form of PMD. He was diagnosed with PMD at the age of 3 months, when he was found to display poor head control and nystagmus. Spastic quadriparesis was evident at 4 years of age, with choreoathetotic movements beginning at the age of 8–10 years. He appeared alert and attentive and was nonverbal but exhibited guttural vocalizations. A missense mutation, c.643 C > T (p.Pro215Ser), was identified in exon 5 of the *PLP1* gene, which has been reported previously (Gencic et al., 1989).

Establishment and Characterization of iPSCs Derived from PMD Patients

Human iPSCs were established via the retroviral transduction of four transcription factors (*SOX2*, *OCT4*, *KLF4*, and *c-MYC*) into dermal fibroblasts (Takahashi et al., 2007). A total of 52 and 34 iPSC clones were established from PMD1 and PMD2 samples, respectively. The established iPSC clones were evaluated based on the typical morphology of colonies similar to human embryonic stem cells (ESCs), as well as the expression of pluripotent markers via immunocytochemistry (NANOG and OCT4; Figure 1D), silencing of retroviral transgenes through quantitative RT-PCR (Figure 1E), and efficient differentiation into neural cells via embryoid body (EB) formation. We finally selected three clones each for PMD1 (1-7, 1-15, and 1-27) and PMD2 (2-6, 2-10, and 2-22) for further analyses. The differentiation potentials of these selected iPSC clones were confirmed through teratoma formation assays (ectoderm: neural rosettes and pigmented epithelium, endoderm: goblet cells, and mesoderm: bones and cartilage; Figure 1F). Moreover, the mutations in the *PLP1* gene (PMD1 [c.757 T > A] and PMD2 [c.643 C > T]) were confirmed in human dermal fibroblasts (HDFs) and all of the selected iPSC clones via pyrosequencing analysis (Figure 1G).

Regarding the control iPSCs, we used age-matched control iPSCs established from 8-month-old (TIG121) and 16-year-old (WD39) healthy individuals, corresponding to the PMD-iPSCs established from 1-year-old and 20-year-old patients, respectively, as well as 201B7, which is a widely used control iPSC clone.

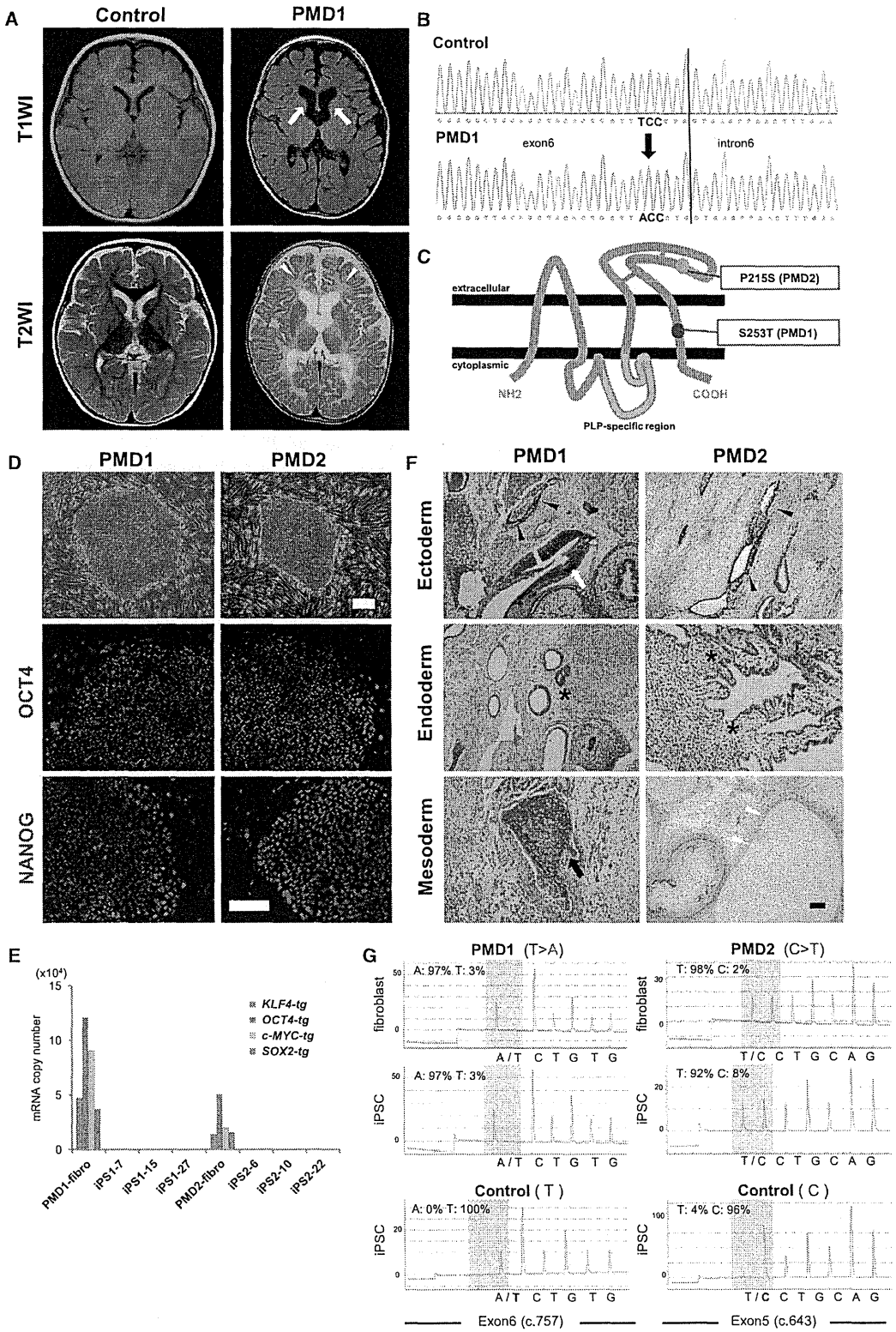

(legend on next page)

Both Control and PMD iPSCs Induce Oligodendrocyte Lineage Cells In Vitro

Based on the previously reported methods for inducing OLs from human ESCs and iPSCs (Hu et al., 2009; Izrael et al., 2007; Kang et al., 2007), we established our own culture protocol to induce OLs by modifying previously established protocols for efficiently differentiating human ESCs and iPSCs into neural stem/progenitor cells (NS/PCs) as neurospheres through EB formation (Nori et al., 2011; Okada et al., 2008). First, dorsomorphin (a bone morphogenetic protein signal inhibitor), SB431542 (a transforming growth factor β [TGF-β] receptor inhibitor), and BIO (a GSK3 inhibitor) were added during the early phase of EB formation to facilitate differentiation into NS/PCs more efficiently. Quantitative RT-PCR analysis of the expression of the NS/PC marker *SOX1* in EBs revealed a significantly higher induction efficiency of NS/PCs in our protocol with DSB (DSB: dorsomorphin, SB431542, and BIO) compared with those in our previously established methods (control, DSB−) or those in the previously reported dual Smad inhibition with DS (Figure 2B). We also added retinoic acid for caudalization and purmorphamine (Sonic hedgehog agonist) for ventralization during EB formation until EB dissociation. Then, the dissociated EBs were cultured in suspension to form neurospheres in proliferation medium supplemented with factors that promote the commitment and proliferation of OL lineage cells (Shimada et al., 2012). For adherent differentiation, neurospheres were cultured in differentiation medium supplemented with factors that promote the commitment of OL lineage cells as indicated in the Experimental Procedures (Figure 2A). From the quantitative RT-PCR analysis in this protocol, the pluripotent marker (*NANOG*) was notably downregulated in the EB stage, and other lineage markers (mesodermal and endodermal markers, such as *BRACHYURY* and *SOX17*) were not detected in any stage. The NS/PC marker (*SOX1*) was upregulated in the EB and neurosphere stages and gradually downregulated after adherent differentiation (differentiation stage; Figure 2C). The expression profiles were similar between the control, PMD1, and PMD2 iPSCs (Figure S1A available online). To reveal the differentiation potentials of neurospheres, we performed immunocytochemistry of differentiated neurospheres for markers of neurons (βIII tubulin), astrocytes (GFAP), and oligodendrocytes (O4; Figures 2E and 2F) and a time course analysis of the expression levels of neuronal and glial markers through quantitative RT-PCR (Figure 2D). The expression profiles were similar between the control and PMD1 and PMD2 cells (Figure S1B). Based on these analyses, we confirmed the differentiation potentials of the iPSCs into three neural lineage cells and the reproducibility of our differentiation protocol. Regarding the differentiation potentials of OL lineage cells, all PMD-iPSCs and control iPSCs were able to induce platelet-derived growth factor receptor α (PDGFRα)$^+$-OL progenitor cells (OPCs), O4$^+$-immature OLs (immature OLs), and myelin basic protein (MBP)$^+$-mature OLs (mature OLs) with typical morphologies (Figure 3B). OPCs were also positive for NG2 (Figure 3A). In contrast, myelin protein zero (MPZ)-positive cells, a major structural protein of peripheral myelin, could not be detected, indicating that these cells were oligodendrocytes, but not schwann cells.

After 55–70 days in vitro (DIV), OPCs were observed in 86.3% of the colonies of control cells and 95.1% and 90.5% of the colonies of PMD1 and PMD2 cells, respectively. At 70–85 DIV, immature OLs were observed in 77.8% of control colonies and 93.8% and 93.8% of the colonies of PMD1 and PMD2 cells, respectively. At 80–95 DIV, mature OLs were observed in 74.9% of the colonies of control cells and 93.8% and 89.2% of the colonies of PMD1 and PMD2 cells, respectively (Figure 3C). No significant

Figure 1. Features of the PMD Patients and Characterization of iPSCs

(A) MRI images of the brains of patient PMD1 (right) and an age-matched control (left). Mild and diffuse atrophy of the brain, dilatation of the ventricles (open arrow), and diffuse high-intensity signals in the white matter (open arrowhead) are shown. T1WI, T1-weighted images; T2WI, T2-weighted images.

(B) Direct sequencing analysis of genomic DNA from PMD1's leukocytes showed a missense mutation c.757 T > A (p.Ser253Thr) in exon 6 of the *PLP1* gene.

(C) Schematic representation of the mutation sites in PMD1 and PMD2.

(D) Representative morphology of iPSC colonies (above) and immunochemical analysis of pluripotent markers, NANOG and OCT4 (below). The scale bars represent 200 μm.

(E) Quantitative RT-PCR analysis of the expression of retroviral transgenes in established PMD iPSC clones. Data are presented as the mRNA copy numbers for each transgene divided by those for *β-actin*.

(F) Representative H&E staining of teratomas derived from established PMD iPSC clones. Teratomas were formed via the injection of undifferentiated iPSCs into the testes of NOD/SCID mice. Open arrow, neural rosettes. Arrowhead, pigmented epitheliums. Asterisks, goblet cells. Arrow, bones. Open arrowhead, cartilage. The scale bars represent 200 μm.

(G) Representative pyrosequencing analysis of the mutations in the *PLP1* gene in fibroblasts and iPSCs. Identical mutations to those observed in the patients' fibroblasts (PMD1, 757 T > A; PMD2, 643 C > T) were confirmed in all the iPSC clones.

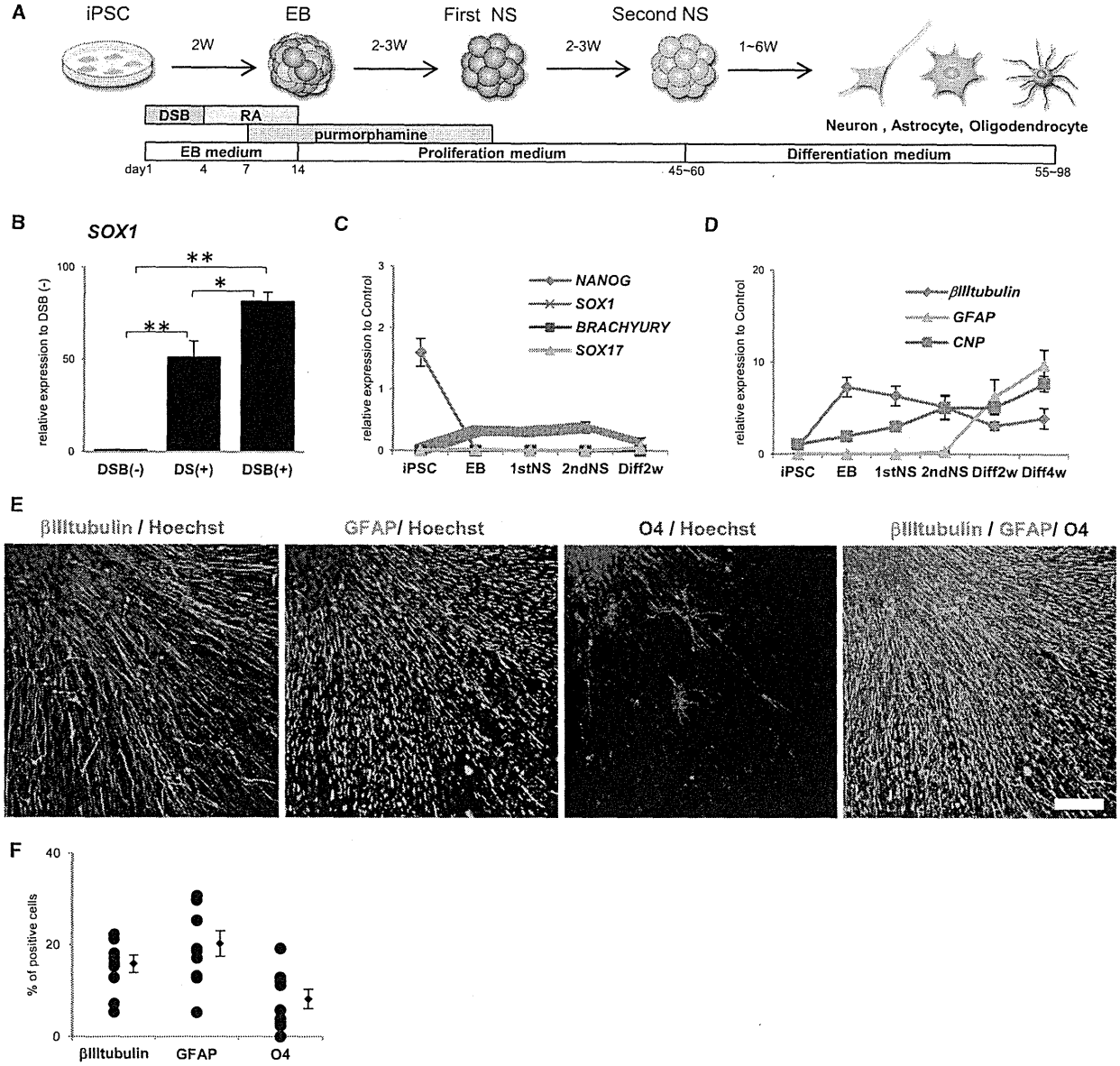

Figure 2. Differentiation Potential of Human iPSCs

(A) Schematic presentation of the protocols for OL differentiation from hiPSCs. DSB, dorsomorphine (D), SB431542 (S), and BIO (B); RA, retinoic acid; NS, neurospheres.

(B) Quantitative RT-PCR analysis of *SOX1* expression in EBs, suggesting a significantly higher induction efficiency of NS/PCs in EBs in our protocol with DSB (DSB: dorsomorphin, SB431542, and BIO) compared with those in our previously established methods (control, DSB−) or those in the previously reported method with dual Smad inhibition (DS) ($n = 3$, mean ± SEM; independent experiments; $^{*}p < 0.05$; $^{**}p < 0.01$; t test).

(C) Quantitative RT-PCR analysis of the expression of cell-type-specific markers at each differentiation stage. *NANOG* (a pluripotent marker) was readily downregulated in the EB stage. Other lineage markers (mesodermal and endodermal markers, such as *BRACHYURY* and *SOX17*) were not detected in any stage. *SOX1* was upregulated in EB and neurosphere stage in control iPSC clones (201B7, WD39, and TIG121; $n = 3$; mean ± SEM; independent experiments).

(D) Quantitative RT-PCR analysis of differentiated neurospheres for the markers of neurons (*βIII tubulin*), astrocytes (*GFAP*), and oligodendrocytes (*CNP*) in control iPSC clones (201B7, WD39, and TIG121; $n = 3$; mean ± SEM; independent experiments).

(legend continued on next page)

differences were detected in either control or PMD with regard to OL lineage differentiation efficiency.

To examine the proportion of immature and mature OL lineage cells, we performed immunocytochemistry for OLIG2, PDGFRα, and MBP after 2 or 4 weeks differentiation of control-iPSC-derived second neurospheres containing more than 40 OLIG2-positive cells and counted the number of marker-positive cells (Figures 3D and 3E). After 2 and 4 weeks of differentiation, OLIG2$^+$ and PDGFRα$^+$ OPCs were abundantly observed. After 4 weeks of differentiation, small numbers of MBP$^+$ mature OLs appeared.

Involvement of ER Stress in PMD

Previous in vitro transfection studies in nonglial cells have indicated that various PLP1 mutants accumulate in the ER immediately after translation, in contrast to the distribution of wild-type PLP1 at the plasma membrane (Gow et al., 1994; Gow and Lazzarini, 1996; Thomson et al., 1997). Therefore, we next examined the expression of PLP1 proteins via immunocytochemistry. When stained with anti-PLP1 and MBP antibodies, the membrane protein PLP1 was observed to be dispersed into the processes of OLs and to colocalize with MBP in control iPSC-derived mature OLs. However, in PMD1 and PMD2 iPSC-derived mature OLs, PLP1 protein staining was not observed in the OL processes; instead, PLP1 protein staining localized to the perinuclear cytoplasm (Figure 4A). Thus, we also performed staining for the ER marker KDEL and found that the mislocalized PLP1 proteins colocalized with KDEL (Figures 4A and 4B). All of the control iPSC-derived OLs showed staining for PLP1 proteins in the processes of mature OLs, whereas all of the PMD iPSC-derived mature OLs only exhibited PLP1 protein localization in the ER. These results suggest that mutant PLP1 proteins accumulated in the ER and triggered ER stress in mature OLs derived from PMD-iPSCs.

We next examined the expression of ER stress markers in OLs. O4$^+$ cells were isolated from both the PMD and control iPSC-derived differentiated cells 4 weeks after the attachment of the second neurospheres via magnetic-activated cell sorting (MACS) using an anti-O4 antibody. The purified O4$^+$ cells underwent quantitative RT-PCR to determine the expression of ER stress markers (*BIP*, *CHOP*, and spliced *XBP1*). No significant differences were detected between the control and PMD iPSC-derived OLs regarding the expression of ER stress markers under default conditions (Figure 4C). Therefore, we next examined the susceptibility of the iPSC-derived OLs to the extrinsic ER stress induced by treatment with a low concentration of tunicamycin 50 nM for 6 hr (known as an ER-stress inducer). The results showed that the expression of all ER-stress markers was significantly increased in tunicamycin-treated O4$^+$ cells relative to untreated O4$^+$ cells in PMD1 (Figure 4D). This result suggested that a higher susceptibility to ER stress was observed in PMD1 iPSC-derived OLs than in those derived from control and PMD2 iPSCs.

We next treated the iPSC-derived OLs with a higher concentration of tunicamycin 100 nM for 6 hr and examined the expression levels of ER stress markers. PMD2 iPSC-derived OLs showed significantly higher expression levels of spliced *XBP1*, the most sensitive ER stress marker, than control iPSC-derived OLs (Figure 4E). No significant differences were detected in the expression levels of *BIP* and *CHOP* between control and PMD2. Taken together, these results suggest that ER stress is involved in the pathogenesis of the PMD patients with PLP1 missense mutations, and a higher susceptibility to ER stress was observed in PMD1 iPSC-derived OLs than in those derived from PMD2, which is consistent with the more severe phenotypes of the PMD1 patient compared with the PMD2 patient.

Increased Apoptosis Is Observed in PMD iPSC-Derived Oligodendrocytes

In addition to their susceptibility to ER stress, the PMD iPSC-derived OLs showed significant morphological differences, as revealed by O4 staining, such as scattered O4 staining in their processes compared with control iPSC-derived OLs, which exhibited uniform O4 staining in their processes (Figure 5A). Thus, to investigate the apoptotic processes of PMD iPSC-derived OL lineage cells, we examined the expression of cleaved caspase-3 (apoptotic marker) in O4$^+$-immature OLs and MBP$^+$-mature OLs via immunostaining. Some of the PMD iPSC-derived OLs that showed scattered O4 staining in their processes were positive for cleaved caspase-3 (Figure 5B). The numbers of cleaved caspase-3$^+$ cells in both PMD1 and PMD2 iPSC-derived immature OLs and mature OLs were significantly increased compared with those derived from control iPSCs (Figure 5C). We next performed immunocytochemistry for KI67 and OLIG2. We found that the proportion of OLIG2$^+$ cells and KI67$^+$ cells among OLIG2$^+$ cells were unchanged between PMD and control samples, suggesting that the compensatory proliferation of OPCs for increased apoptosis in PMD iPSC-derived OLs is unlikely (Figures S2A and S2B). Therefore, although

(E) Representative low-magnification images of the immunocytochemistry of three neural lineage cells (neurons: βIII tubulin; astrocytes: GFAP; oligodendrocytes: O4). The scale bar represents 100 μm.
(F) Quantitative analysis of the percentages of three neural lineage cells in control-iPSCs (201B7, WD39, and TIG121)-derived neurospheres (n = 9; mean ± SEM; independent experiments).

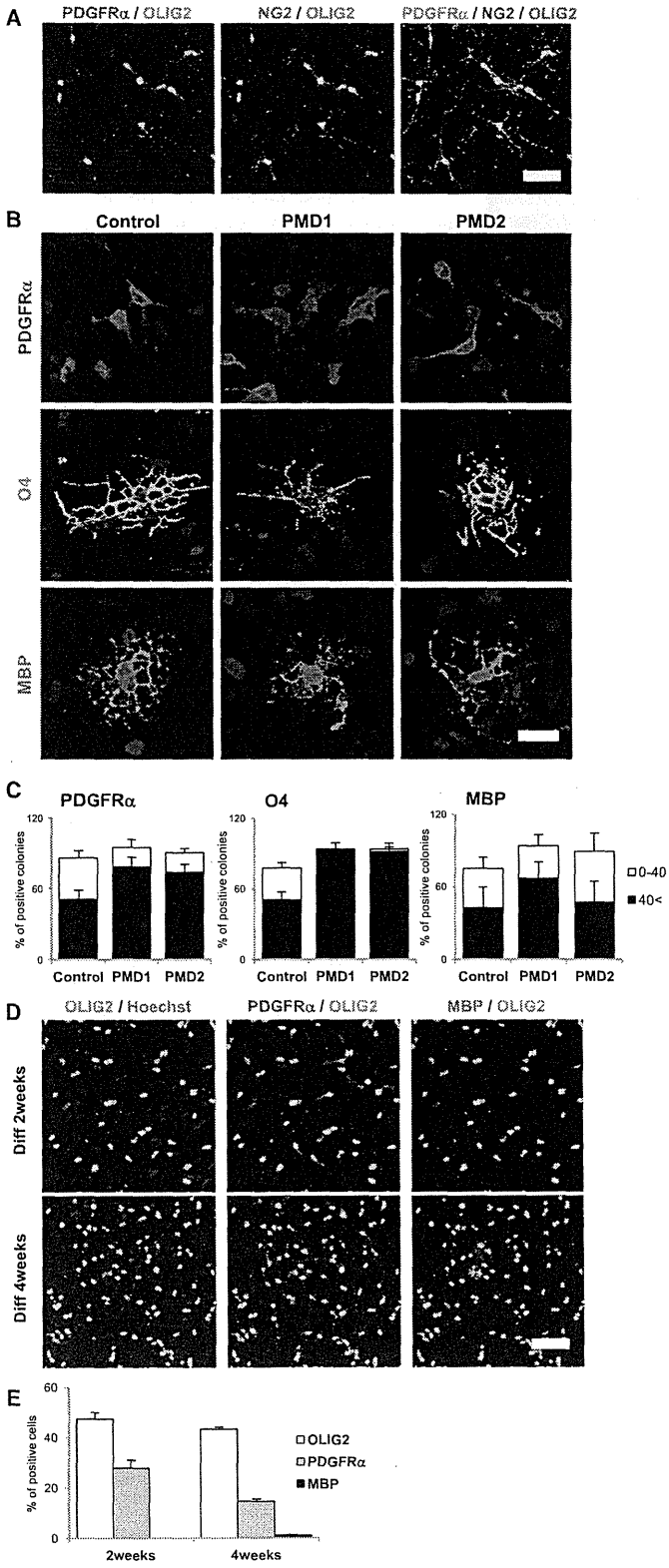

Figure 3. Differentiation Potential of Human iPSCs into Oligodendrocytes

(A) Representative image of immunocytochemistry for OPC markers (PDGFRα and NG2). OPCs were positive for both PDGFRα and NG2. The scale bar represents 50 μm.

(B) Representative image of immunocytochemistry of differentiated neurospheres using markers for OL lineage cells. Both control and PMD iPSCs differentiated into PDGFRα$^+$-OL progenitor cells (OPCs), O4$^+$-immature OLs (immature OLs), and MBP$^+$-mature OLs (mature OLs). The scale bar represents 20 μm.

(C) Quantitative analysis of the differentiation efficiency into OL lineage cells. The numbers of neurosphere colonies containing more than 40 marker-positive cells (≥40 cells; oligodendrocyte [++]), those containing less than 40 marker-positive cells (1–39 cells oligodendrocyte [+]), and those without marker-positive cells (oligodendrocyte [−]) were counted and are presented as the percentage of total neurosphere colonies. Oligodendrocyte (++) neurosphere colonies and oligodendrocyte (+) neurosphere colonies are indicated by black and white bars, respectively (PDGFRα, n = 6; O4, n = 6; MBP, n = 4; mean ± SEM; independent experiments). No significant difference was detected among control (201B7, WD39, and TIG121) and PMD iPSCs (PMD1-7, PMD1-15, and PMD1-27 and PMD2-6, PMD2-10, and PMD2-22)-derived OL lineage cells ($p > 0.05$; Mann-Whitney's U test).

(D) Representative image of immunocytochemistry for OLIG2, PDGFRα, and MBP after 2 or 4 weeks differentiation of control-iPSC-derived second neurospheres containing more than 40 OLIG2-positive cells. The scale bar represents 50 μm.

(E) Quantitative data of the percentages of PDGFRα$^+$ cells/OLIG2$^+$ cells and MBP$^+$ cells/OLIG2$^+$ cells (after 2 or 4 weeks of differentiation) in control-iPSC (201B7, WD39, and TIG121)-derived neurospheres containing more than 40 OLIG2-positive cells. (n = 3; mean ± SEM; independent experiments). After 2 and 4 weeks of differentiation, OLIG2$^+$ and PDGFRα$^+$ OPCs were abundantly observed. After 4 weeks of differentiation, small numbers of MBP$^+$ mature OLs appeared.

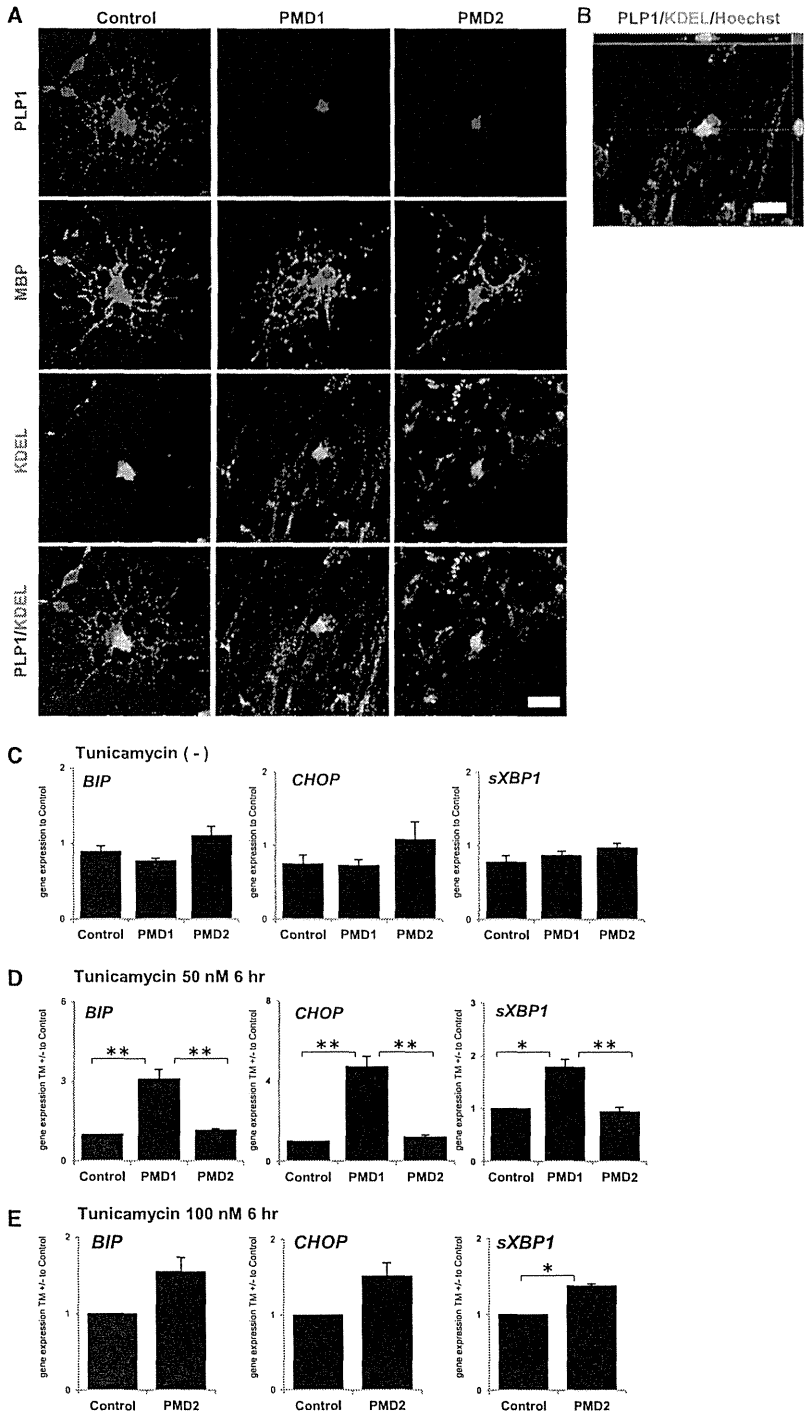

Figure 4. Involvement of ER Stress in PMD-Derived Oligodendrocytes

(A) Representative immunocytochemistry image for PLP1, the OL marker MBP, and the ER marker KDEL. In the control iPSC-derived mature OLs, the PLP1 protein localized to both the ER (KDEL) and membrane, whereas in the PMD iPSC-derived OLs, the mutant PLP1 protein only localized to the ER. The scale bar represents 20 μm.

(B) Three-dimensional image of mature OLs derived from PMD1 iPSCs showing colocalization of the mutant PLP1 protein and KDEL via confocal laser scanning microscopy. The scale bars represent 20 μm.

(C) Quantitative RT-PCR analyses of the expression of ER stress markers in $O4^+$ cells. The data are presented as the expression relative to that in iPSCs. No significant differences were observed between the control iPSC (201B7, WD39, and TIG121) and PMD iPSC (PMD1-7, PMD1-15, and PMD1-27 and PMD2-6, PMD2-10, and PMD2-22)-derived cells (n = 5; mean ± SEM; independent experiments; t test).

(D) Quantitative RT-PCR analyses of the expression of ER stress markers in tunicamycin-treated (50 nM; 6 hr) $O4^+$ cells relative to untreated $O4^+$ cells. A higher level of stress susceptibility was detected in PMD1 (PMD1-7, PMD1-15, and PMD1-27) than in control (201B7, WD39, and TIG121) and PMD2 (PMD2-6, PMD2-10, and PMD2-22; n = 5; mean ± SEM; independent experiments; *p < 0.05; **p < 0.01; Mann-Whitney's U test).

(E) Quantitative RT-PCR analyses of the expression of ER stress markers in tunicamycin-treated (100 nM; 6 hr) $O4^+$ cells relative to untreated $O4^+$ cells. PMD2 iPSC (PMD2-6, PMD2-10, and PMD2-22)-derived OLs showed significantly higher expression levels of spliced *XBP1* than control iPSC (201B7, WD39, and TIG121)-derived OLs (n = 3; mean ± SEM; independent experiments; *p < 0.05; t test).

the differentiation efficiency into oligodendrocyte lineage cells was unchanged between PMD and control (Figure 3C), considering that anti-O4 and anti-MBP antibodies stain both apoptotic and live OLs (Figures 5A and 5C), the increased levels of apoptosis resulted in decreased numbers of live OLs in PMD iPSC-derived cultures.

Because previous reports have indicated the neurotrophic actions of PLP1 (Griffiths et al., 1998; Yin et al.,